

Si-, Ge-, Sn-Based Anode Materials for Lithium-Ion Batteries: From Structure Design to Electrochemical Performance

Weihan Li, Xueliang Sun, and Yan Yu*

As state-of-the-art rechargeable energy-storage devices, lithium-ion batteries (LIBs) are widely applied in various areas, such as storage of electrical energy converted from renewable energy and powering portable electronic devices and electric vehicles (EVs). Nevertheless, the energy density and working life of current commercial LIBs cannot satisfy the rapid development of these applications. It is urgently required that the electrochemical performance of LIBs, which is mainly determined by the electroactive electrode materials, is improved. However, commercial graphite-based anode materials deliver a relatively low theoretical capacity of 372 mA h g^{-1} , severely hindering the increase of the energy density of LIBs. Recently, M-based anode (M represents Si, Ge, and Sn) materials have attracted great attention due to their high theoretical capacity and reasonable anodic voltage. However, the application of M-based anode materials is seriously limited by a series of several critical problems, such as poor kinetics and huge volume change on cycling. Here, these fundamental problems leading to poor electrochemical performance are discussed, and a series of reasonable nanostructures for M-based anodes with improved electrochemical performance is summarized, demonstrating that the dimensional control in structure design plays a critical role for solving these problems.

non-renewable character of fossil fuels.^[1,2] To solve this tough issue, sustainable renewable energy, such as wind energy and solar energy, has been studied for decades to gradually replace fossil fuels.^[3,4] Unfortunately, the intermittency of renewable energy resources disturbs direct practical application. In this regard, rechargeable batteries play a crucial key role in storing and delivering the electric energy generated from renewable energy, which is essential to efficient utilization of wind or solar power.^[5–8] Among the current commercial rechargeable batteries, lithium-ion batteries (LIBs) have shown great promise due to their high energy density and long cycle life, when applied to power portable electronic devices (including cellphones, laptops, etc.), showing great promise for application in electric vehicles (EVs) and hybrid EVs.^[9–12] Nevertheless, the gravimetric and volumetric energy density of current commercial LIBs is still very low. It still remains a great challenge for LIBs to meet the requirements for applications in the fields of grid-energy storage and

EVs. In addition, the cycle life of LIBs has been widely tested for application in small-scale energy storage at stable working states, while the electrochemical performance of LIBs applied in large-scale energy storage at unstable energy-conversion states (e.g., renewable energy) is still unknown, and needs further study.^[13–16]

The performance of LIBs, including the energy density, working life, and safety, is mainly determined by the primary functional components, particularly by the electrode materials.^[17] The electrode materials of current commercial LIBs mainly consist of metal oxides or phosphate cathode materials (e.g., LiCoO_2 and LiFePO_4) and graphite-based anode materials.^[18] However, the theoretical capacity of these graphite-based anode materials is only 372 mA h g^{-1} , severely reducing the energy density of LIBs.^[19] To improve the capacity of anode materials, considerable attention has been devoted to alloy-type anode materials, owing to their high specific capacity and safety characteristics.^[20,21] Among various alloy-type anode materials, those based on silicon (Si), germanium (Ge), and tin (Sn) show amazing capacities of 4200, 1625, and 994 mA h g^{-1} , respectively, holding great potential as anode materials for next-generation LIBs.^[13,22–30] However, these anode materials

1. Introduction

At present, fossil fuels are widely utilized to power the world, which, however, causes serious environmental pollution. Furthermore, another serious problem, the energy crisis, is constantly becoming more and more serious, owing to the

Dr. W. Li, Prof. Y. Yu
Key Laboratory of Materials for Energy Conversion
Chinese Academy of Sciences
Department of Materials Science and Engineering
University of Science and Technology of China
Hefei, Anhui 230026, P. R. China
E-mail: yanyumse@ustc.edu.cn

Prof. X. Sun
Department of Engineering
The University of Western Ontario
London, Ontario, Canada

Prof. Y. Yu
State Key Laboratory of Fire Science
University of Science and Technology of China
Hefei, Anhui 230026, P. R. China



DOI: 10.1002/smt.201600037

undergo a huge volume variation during cycling, leading to poor electrochemical performance.^[31,32] In the last few decades, great effort has been made to conquer the obstacles of M (M represents Si, Ge, and Sn) as anode materials for LIBs through rational electrode structure design. Here, we will present a broad overview of the reasonable structure design of these anode materials, focusing on dimensional control in structure design.

2. Advantages and Challenges of Si-, Ge-, and Sn-Based Anode Materials

As shown in **Table 1**, based on the intercalation mechanism, graphite materials can store one lithium atom per six carbon atoms (lithiated to LiC_6), presenting a specific capacity of 372 mA h g^{-1} .^[19,33] Different from the intercalation mechanism of graphite, Si, Ge, and Sn operate based on the alloying mechanism with fully lithiated phase of $\text{Li}_{4.4}\text{M}$, delivering high gravimetric capacities of 4200, 1625, and 994 mA h g^{-1} , respectively, much higher than that of graphite.^[34–38] In addition, superior volumetric capacities of these anode materials, ranging from 7216 to $9786 \text{ mA h cm}^{-3}$, along with the high gravimetric capacities discussed above, make them promising high-energy-density anode materials for LIBs.^[21,39,40] Furthermore, the delithiation potential of commercial graphite is low, $\approx 0.05 \text{ V vs Li/Li}^+$, easily forming Li dendrites at high current density.^[41] The Li dendrites on the surface of anodes are one of the main reasons for the internal short-circuit of LIBs, resulting in serious safety problems, like ignition and explosion.^[42] Fortunately, these M anode materials display more-favorable average delithiation voltage, about $0.4\text{--}0.6 \text{ V vs Li/Li}^+$, which will increase the cut-off voltage to avoid the formation of Li dendrites and improve LIB safety.^[43] Moreover, the delithiation voltage of these M anode materials, compared with other zero-strain anode materials (e.g., $\text{Li}_4\text{Ti}_5\text{O}_{12}$), is relatively low, leading to high working voltage and energy density.^[44,45] In addition, these M anode materials have other merits, such as abundant resource and environmental benignity for Si, and high lithium diffusion coefficient for Ge, and high electronic conductivity for Sn. The advantages of these M anode materials promise huge potential for applications in next-generation LIBs.

However, the practical application of these M anodes is seriously hindered by poor cyclability, as well as by large irreversible capacity loss because of the huge volume change of the anode materials during cycling.^[46,47] As shown in **Table 1**, during lithium alloying, it can take up 4.4 Li atoms for each M atom to form the fully lithiated phases, leading to tremendous volume expansion up to several hundred times being present (e.g., 420% for $\text{Li}_{4.4}\text{Si}$ and 370% for $\text{Li}_{4.4}\text{Ge}$).^[23] The continuous up-take and release of Li atoms in these M anodes on cycling will bring about large volume expansion/contraction and enormous stress inside the anode particles, leading to the cracking and even pulverization of the anode particles and the fracture of electronic conductive network around electroactive M particles.^[48] Generally, the pulverized anode particles can not participate in the following electrochemical reaction, leading to rapid capacity fading. The



Weihan Li completed his doctorate in material sciences under the supervision of Prof. Yan Yu at the University of Science and Technology of China, Hefei, in 2016. He is currently a postdoctoral fellow in the Department of Mechanical and Materials Engineering at the University of Western Ontario with Prof. Xueliang Sun as his Principal Investigator. His research interests include synthesis and application of nanomaterials for lithium-ion batteries and sodium-ion batteries.



Xueliang (Andy) Sun is a Canada Research Chair in Development of Nanomaterials for Clean Energy, Fellow of the Royal Society of Canada and Canadian Academy of Engineering and Full Professor at the University of Western Ontario, Canada. Dr. Sun received his Ph.D. in materials chemistry in 1999 from the University of Manchester, UK, which he followed up by working as a postdoctoral fellow at the University of British Columbia, Canada and as a Research Associate at L'Institut National de la Recherche Scientifique (INRS), Canada. His current research interests are focused on advanced materials for electrochemical energy storage and conversion, including electrocatalysis in fuel cells and electrodes in lithium-ion batteries and metal–air batteries.



Yan Yu is a professor of material science at the University of Science and Technology of China (USTC). She received her Ph.D. in materials science at USTC in 2006. From 2007 to 2008, she worked as a postdoctoral at Florida International University. After that she received Humboldt Research Fellow from the Alexander von Humboldt Foundation and worked at the Max Planck Institute for Solid State Research in Stuttgart, Germany. Her current research interests include the design of novel nanomaterials for clean energy, especially for batteries, and the fundamental science of energy-storage systems.

Table 1. Comparison of C and Si, Ge, and Sn anode materials.

	Density [g cm ⁻³]	Lithiated phase	Theoretical gravimetric capacity [mA h g ⁻¹]	Theoretical volumetric capacity [mA h cm ⁻³]	Potential vs Li/Li ⁺ [V]	Volume variation [%]
C (graphite)	2.25	LiC ₆	372	837	0.05	12
Si	2.33	Li _{4.4} Si	4200	9786	0.4	420
Ge	5.32	Li _{4.4} Ge	1625	8645	0.5	370
Sn	7.26	Li _{4.4} Sn	994	7216	0.6	260

dramatic morphology variation of electrodes can detach parts of electrodes from the conductive network and even peel off entire electrodes from the current collectors, contributing to more-severe capacity fading. In addition, the volume variation and cracking of anode materials will affect the solid electrolyte interface (SEI) layer coated on the surface of anode particles.^[49,50] The SEI layer is formed because of the decomposition of the organic electrolyte during the lithiation process below ≈ 1 V vs Li/Li⁺, whose composition depends on the composition of electrolytes and additives, such as lithium alkyl carbonates (ROCO₂Li), Li₂O and LiF, and poly(ethylene oxide) (PEO).^[51–53] A well-formed SEI layer can separate the electrodes from the electrolyte, inhibiting the further side electrochemical reaction of the electrolyte on the surface of the electrodes and guaranteeing a long cycle life via allowing effective transport of lithium ions through the SEI layer and subsequent lithium intercalation or alloying reactions with the electrodes,^[22] whereas the huge volume change of electrodes during cycling will lead to breakdown of the SEI layer, which cannot withstand the volume variation of the underlying electrodes.^[13] The fresh surface of these M anodes will be exposed to the organic electrolyte, leading to on-going growth of the SEI layer to be very thick, which will impede transport of ions/electrons and damage the electrochemical performance.^[22] A lot of the electrolyte will also be consumed in the formation of a thick SEI layer, which could be fatal for commercial LIBs if the electrolyte is completely consumed.^[54]

Based on the above discussion, the huge volume variation of these M anode materials is the origin of the rapid fading of the capacity. As the volume change on cycling cannot be avoided, the key solutions to improve the cyclability should be to prevent the loss of electrical contact in the electrodes and retain the stability of the SEI layer. Considering the practical application discussed above, cyclability, capacity decay rate, and rate performance are three key metrics to evaluate the materials. To improve the three kinds of electrochemical performance of M anode materials, numerous strategies have been applied, including rational structure design. In the next sections, we present various kinds of reasonable structure design to solve the problems discussed above, focusing on dimensional control in structure design. Among the efficient methods, fabrication of nanomaterials is one widely applied strategy to improve the electrochemical performance of M anode materials.^[8] Nanomaterials can be divided to three main types, including zero-dimensional (0D), one-dimensional (1D), and two-dimensional (2D) nanostructures, based on the size of materials in the three dimensions. For 0D nanomaterials, the size of this type material should be 1–100 nm and the

number of dimensions less than 100 nm are three, such as quantum dots. In this manner, the 1D and 2D nanomaterials have one and two dimensions outside of the nanometer-scale size range, respectively. Furthermore, the 3D nanomaterials usually consist of 0D, 1D or 2D nanomaterials, like 3D porous graphene foam.^[55] The structural difference among these nanomaterials will affect the electrochemical performance of the M anode materials. Firstly, the huge volume change of M anode materials with different nanostructures during cycling will be different, owing to the size in different dimensions. Secondly, the electron- and ion-transport pathways along the nanomaterials with different dimensions are different, resulting in special electronic or ionic conductivities. These two parts are crucial to the electrochemical performance of M anode materials.

3. Reasonable Structure Design of Si-, Ge-, and Sn-Based Anode Materials

3.1. Nanoparticle Anode Materials (Zero-Dimensional (0D) Structures)

Benefiting from nanosize effects, the fabrication of M nanoparticles has been proven to be one effective strategy to improve the cyclability of M anode materials.^[22,56,57] To find out the direct evidence of cycling stability of M nanoparticles, Liu and co-workers^[58] studied the lithiation process of individual silicon nanoparticles with different diameters through in situ transmission electron microscopy (TEM). As shown in **Figure 1**, for the structure stability during the first lithiation process, the critical particle diameter is about ≈ 150 nm, below which the Si nanoparticles would also undergo volume expansion but without fracture and cracking. Although this work only shows the results during the first lithiation process, not considering continuous volume expansion/contraction during long cycle life, the study suggested that nanosized M particles can bear huge volume change and improve cycle performance.

Based on the critical diameter theory, numerous M nanoparticle anode materials have been studied. Lin et al.^[59] prepared Si nanoparticles through the reduction of SiCl₄ by metallic Mg in molten AlCl₃ at a low temperature of 200 °C. **Figure 2A,B** show the prepared Si nanoparticles with diameter ranging from tens to around 100 nm. Attributed to the reduced mechanical strain of the nanostructured Si particles during cycling, the material showed improved cyclability at a current density of 3 A g⁻¹. Although the Si nanoparticles showed limited capacity retention during the initial 100 cycles,

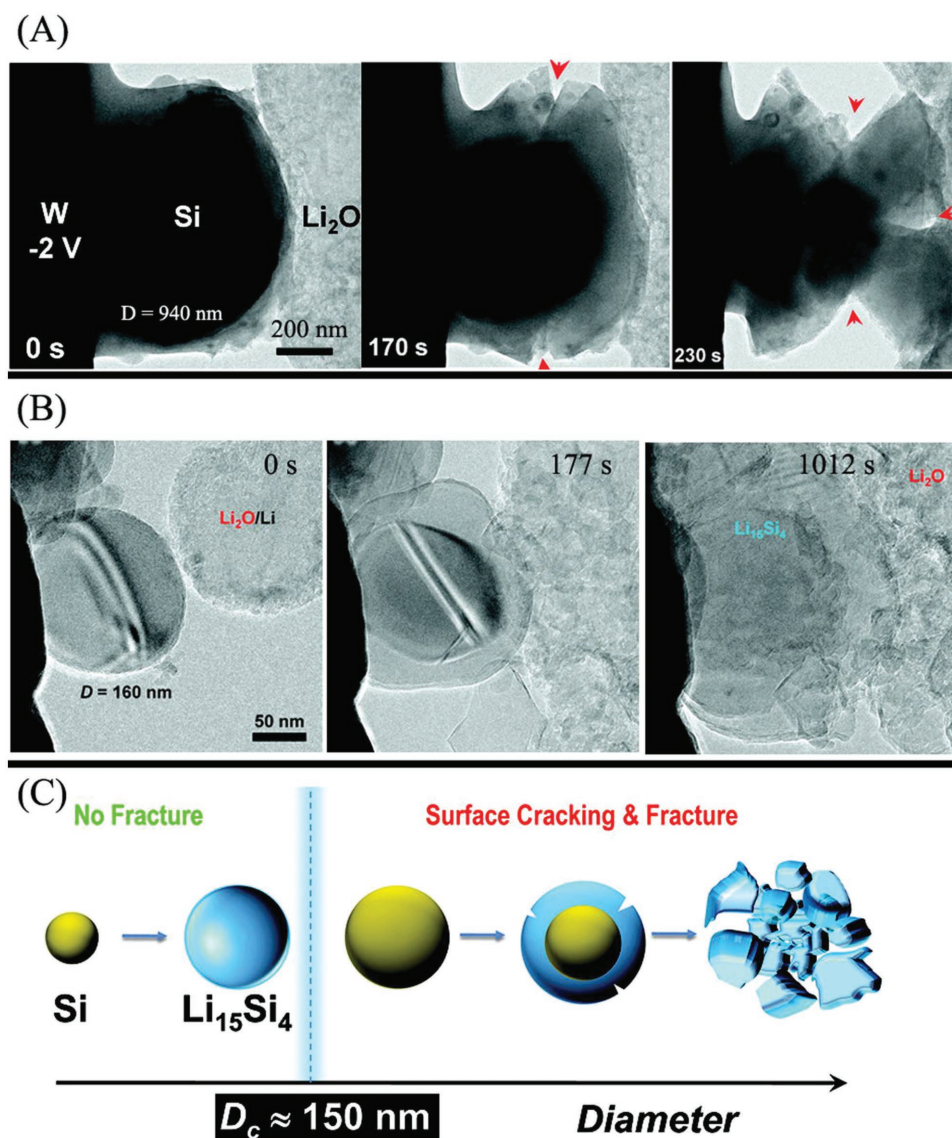


Figure 1. A) TEM images of a large silicon nanoparticle (SiNP) ($D \approx 940$ nm) and a small silicon nanoparticle ($D \approx 160$ nm) at different electrochemical lithiation states. B) Schematic of the critical diameter of Si nanoparticles, above which the particles would crack. Reproduced with permission.^[58] Copyright 2012, American Chemical Society.

the material delivered a high specific capacity of 1180 mA h g^{-1} after 500 cycles with only 0.1% decay per cycle (Figure 2C), suggesting improved cyclability at high current densities. To further improve the structure stability and electrochemical performance, other 0D nanostructured materials based on M anodes have also been intensively studied, including hybrid nanoparticles,^[60,61] hollow nanoparticles,^[62–64] and core-shell-structured particles.^[30,65–68] Xu and co-workers^[60] have synthesized nano-Sn/C composite nanoparticles with nanosized Sn homogeneously dispersed in a spherical carbon matrix through a one-aerosol-spray pyrolysis method (Figure 3A,B). The unique structure can not only alleviate the strain from the volume change ascribed to the Sn nanoparticles but also accommodates the large volume variation through the carbon matrix, leading to excellent capacity retention with no obvious

capacity fading after 130 cycles at 200 mA g^{-1} (Figure 3C,D). Additionally, hollow nanoparticles are an ideal structure design with internal void space to further accommodate the volume change. Chen et al.^[63] presented improved lithium-storage performance for the silver-decorated hollow silicon nanoparticles fabricated through a magnesiothermic reduction process. They display good cyclability with over 93% capacity retention after 100 cycles at 100 mA g^{-1} . To further improve the structural stability to buffer huge volume change, hollow particles with highly porous structure might be a more-suitable strategy. Liu and co-workers^[64] presented a novel design of hollow Ni_3Sn_2 porous microcages. As shown in Figure 4A, the hollow porous microcages consisted of Ni_3Sn_2 nanoparticles with a highly porous structure, crucial to ensuring structural stability during the lithiation process. Figure 4B presents

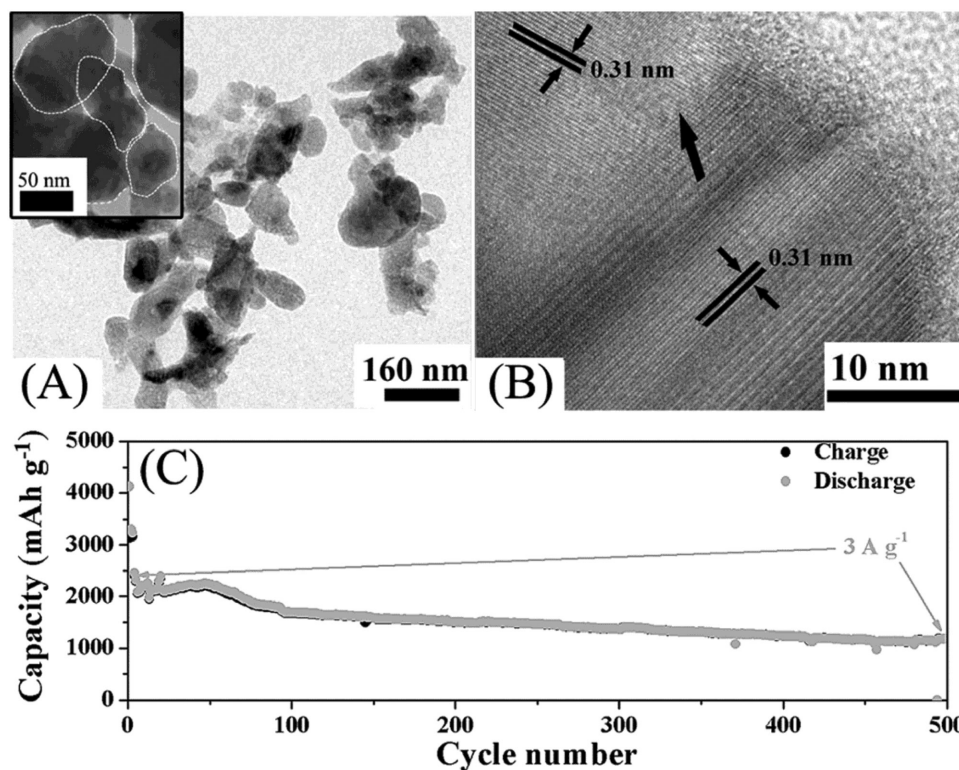


Figure 2. A,B) TEM (A) and HRTEM (B) images of Si nanoparticles. C) Cycle performance of the Si nanoparticles at 3 A g^{-1} , firstly cycled at 0.3 A g^{-1} for 3 cycles. Reproduced with permission.^[59] Copyright 2015, Wiley-VCH.

the structural evolution after the lithiation process. The materials will retain the entire morphology, owing to the sufficient void space inside the hollow microcages. The stable structure during cycling makes the material an excellent anode material for LIBs, delivering 534 mA h g^{-1} after 1000 cycles at 1 C (Figure 4C). Another widely studied 0D structure design is nanoparticles coated with protective layers, including metal and carbon layers. In work by Hu et al.^[67] the typical core-shell structure for Si nanoparticles was presented. They are coated by amorphous SiO_x and carbon layers, $\text{Si}@\text{SiO}_x/\text{C}$, capable of significantly improving the cycling performance.

Besides the traditional design of the core-shell coating structure, the void space between the M particles and carbon layers was further introduced to accommodate the volume change and guarantee stable SEI layers.^[30,68] As shown in Figure 5A,B, Zhang and co-workers^[30] prepared tin nanoparticles (diameter $\approx 100 \text{ nm}$) encapsulated within elastic hollow carbon spheres (diameter $\approx 500 \text{ nm}$, thickness of shells $\approx 20 \text{ nm}$) (TNHCs) with extra void volume between the tin nanoparticles and the carbon shells. During the Li-uptake process, the void space in these TNHCs will accommodate the volume expansion of the lithiated Sn up to $\text{Li}_{4.4}\text{Sn}$, ensuring that the entire structure is intact (Figure 5C). The initial Coulombic efficiency (ICE) is low (the first discharge and charge capacity: 1750 and 1250 mA h g^{-1}), mainly owing to the decomposition of electrolytes to form the SEI layers. In addition, the rapid capacity fading in the first few cycles was mainly ascribed to the pulverization of the inner Sn particles. However, after

that, the capacity became stable at $\approx 550 \text{ mA h g}^{-1}$, owing to the buffering effect of the extra void volume structure inside the carbon shells. Furthermore, this kind of rational structure design has been also successfully extended to micro-sized particles from nanosize particles. Lu and co-workers^[68] designed a nonfilling carbon-coated porous Si-microparticle core-shell structure (nC-pSiMP) with no carbon filled in the pore space of the Si. As shown in Figure 6A, the nonfilling carbon-coating structure could accommodate the huge volume change of Si through the pore space in the microparticles and ensure the stability of the carbon-coating layers, crucial to guaranteeing the stability and thinness of the SEI layers, which was restricted to the outer surface of carbon layers. Figure 6B,C displays scanning electron microscopy (SEM) and TEM images of the nC-pSiMP, fabricated through thermal disproportionation of SiO microparticles to Si nanoparticles embedded in a SiO_2 matrix and subsequent removal of the SiO_2 . As a contributed by the unique structure, the nC-pSiMP with the nonfilling carbon coating showed much better cycling performance than others with an impregnated carbon-coating and non-carbon-coating layers (Figure 6D). The nC-pSiMP showed an initial capacity of $\approx 1798 \text{ mA h g}^{-1}$ at a cycling rate of 0.05C ($1\text{C} = 4200 \text{ mA g}^{-1}$), where the low current density was applied to activate the p-SiMP and form stable SEI layers. After four cycles at 0.05C , the nC-pSiMP was cycled at a higher rate of 0.25C , showing stable capacity retention from the 4th to the 1000th cycle and delivering over 1490 mA h g^{-1} after 1000 cycles.

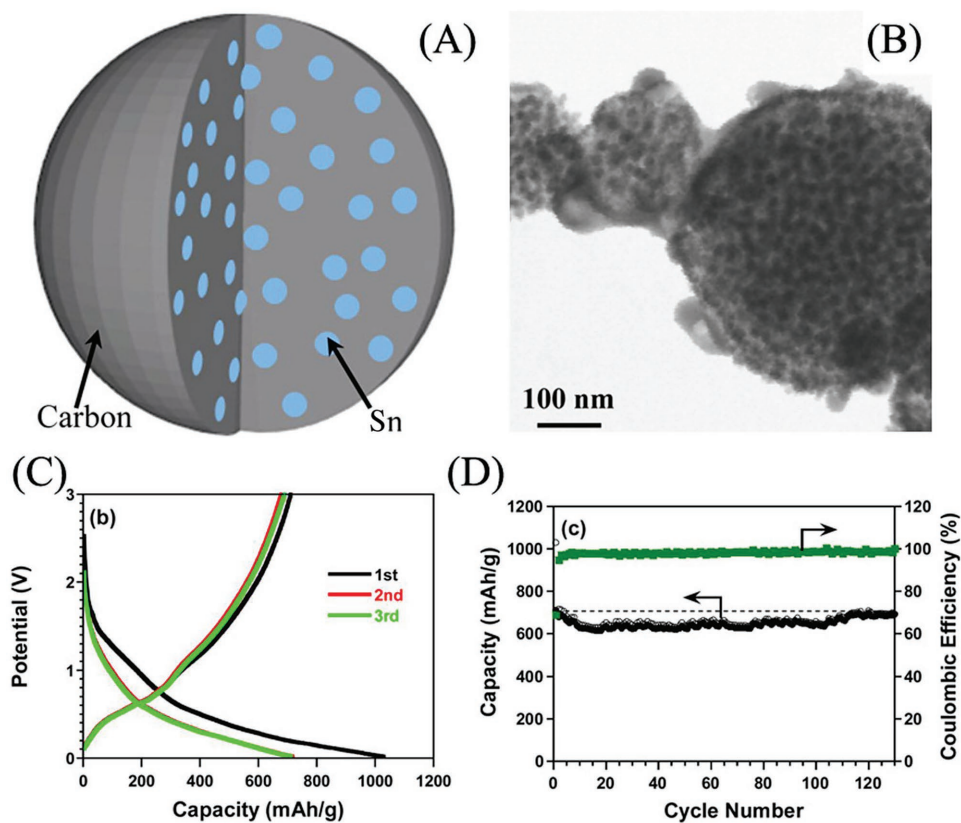


Figure 3. A,B) Schematic diagram (A) and TEM image (B) of the nano-Sn/C composite particles. C,D) Voltage profiles (C) and cycle performance (D) of the nano-Sn/C composite cycled at 200 mA g^{-1} . Reproduced with permission.^[60] Copyright 2013, American Chemical Society.

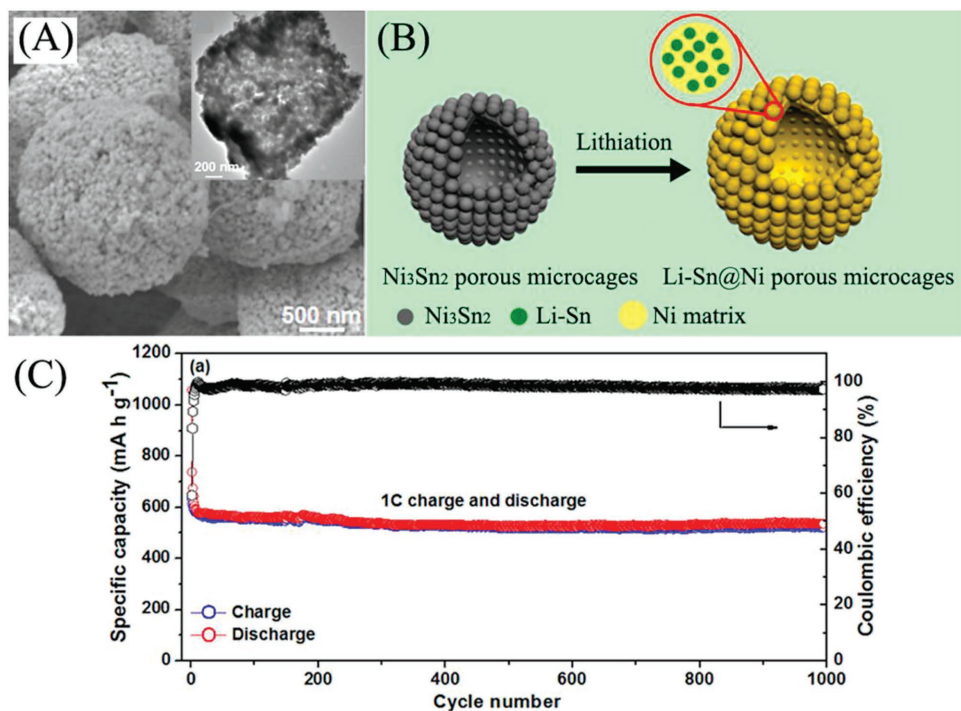


Figure 4. A) Schematic of structural evolution of Ni_3Sn_2 porous microcages after lithiation. B,C) SEM and TEM images (B) and cycle performance at a current density of 1 C (C) for Ni_3Sn_2 porous microcages. Reproduced with permission.^[64] Copyright 2014, American Chemical Society.

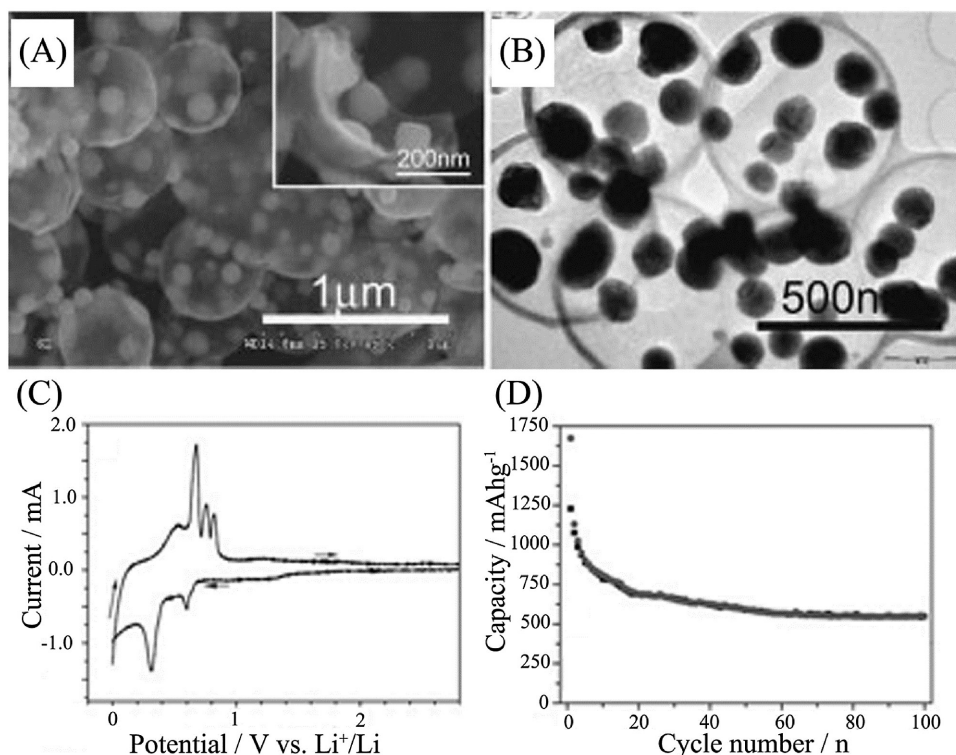


Figure 5. A,B) SEM (A) and TEM (B) images of tin nanoparticles encapsulated elastic hollow carbon spheres (TNHCs). C) Cycle voltammograms of TNHCs with a scan speed of 0.2 mV s⁻¹. D) Cycle performance of of TNHCs cycled at 0.2C. Reproduced with permission.^[30] Copyright 2008, Wiley-VCH.

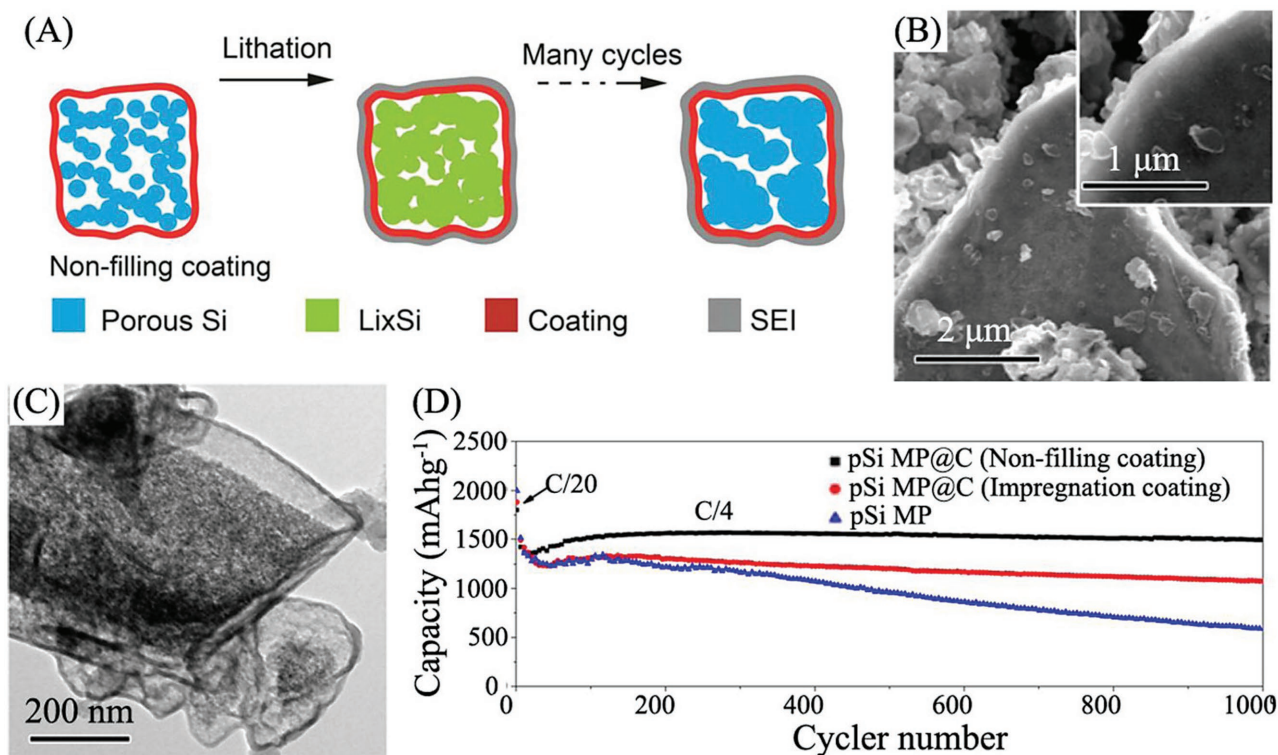


Figure 6. A) Schematic of the structure evolution during cycling of the nonfilling carbon-coated porous silicon microparticle (nC-pSiMP). B,C) SEM (B) and TEM (C) images of the prepared nC-pSiMP. D) Cycle performance of the pSiMPs with different carbon-coating layers. Reproduced with permission.^[68] Copyright 2015, American Chemical Society.

3.2. Nanowire and Nanotube Anode Materials (One-Dimensional (1D) Structures)

Other promising structure design strategies for M anode materials have also been developed, such as one-dimensional (1D) structures (nanowires and nanotubes).^[69] Generally, 1D structures are capable of restricting the mechanical strain during the volume change to low levels in the radial direction to prevent the electrode materials pulverizing. Moreover, along the length direction, the feature of the 1D structure can provide efficient electron-transport pathways, allowing rapid charge transfer. Many groups have fabricated a large number of 1D-structured M anode materials to improve the electrochemical performance, including 0D M nanoparticles encapsulated in 1D nanofibers (NPs@NFs),^[24,25,70–75] M nanowires (NWs) and nanotubes (NTs),^[23,76–81] and core-shell NWs or NTs.^[82–93]

3.2.1. 0D Nanoparticles Encapsulated in 1D Nanofibers (NPs@NFs)

Hwang and co-workers^[72] prepared Si nanoparticles (core) well wrapped by carbon shells, denoted as SiNP@C, by coaxial electrospinning technology. **Figure 7A,B** display the morphology of the SiNP@C, 1D nanofibers (diameter of $\approx 1 \mu\text{m}$) with the Si NPs encapsulated within the core section, uniformly coated by the carbon shell. As presented in **Figure 7C**, the structural integrity after cycling is confirmed by the stability of the structure and the SEI layers of the SiNP@C during the reversible

lithiation/delithiation processes and by the improved cycle performance. After activation at a lower current density of 0.1C for 5 cycles, the fibers can deliver a capacity of 721 mA h g^{-1} after 300 cycles at 3C with negligible capacity loss (**Figure 7D**). Similarly, Li et al.^[25] and Liu et al.^[24] applied the more-convenient single-nozzle electrospinning and the solvent thermal methods to obtain their 1D nanostructures, respectively. As expected, the prepared 0D Ge nanoparticles embedded in carbon nanofibers lead to an enhancement of the cyclability and rate capability. Although the NPs@NFs structure is similar to the M nanoparticles with coating layers discussed above, the 1D construction can also enhance electronic transport along the 1D conductive matrix.

On the other hand, engineering an empty space in the NPs@NFs structure allows further volume expansion of NPs on cycling.^[75] Yu and co-workers^[73,74] have prepared two kinds of Sn nanoparticles dispersed in carbon nanofibers with extra empty space by electrospinning. **Figure 8A,C** display the two types of Sn-C composite nanofibers. One is Sn nanoparticles encapsulated in porous multichannel carbon microtubes (SPMCTs), and the other is Sn@carbon nanoparticles encapsulated in bamboo-like hollow carbon nanofibers. By introducing a soft-template, poly(methyl methacrylate) (PMMA) and mineral oil into the electrospinning precursor solutions as sacrificial templates, respectively, empty space will be formed between the Sn nanoparticles and the carbon layers in the two structures. The void volume provides sufficient space to accommodate the volume variation of the Sn nanoparticles during cycling and the stability of the SEI layers is maintained, which is

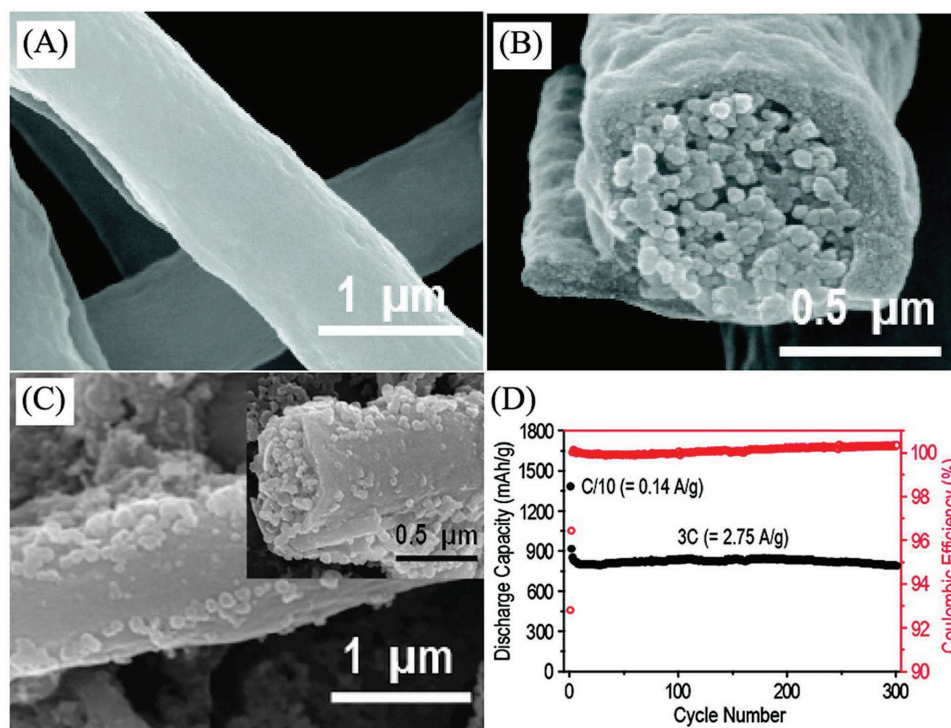


Figure 7. A,B) SEM images of the SiNP@C nanofibers. C) SEM images of the SiNP@C nanofibers after 50 cycles. D) Cycle performance of SiNP@C nanofibers at 2.75 A g^{-1} (3C). Reproduced with permission.^[72] Copyright 2012, American Chemical Society.

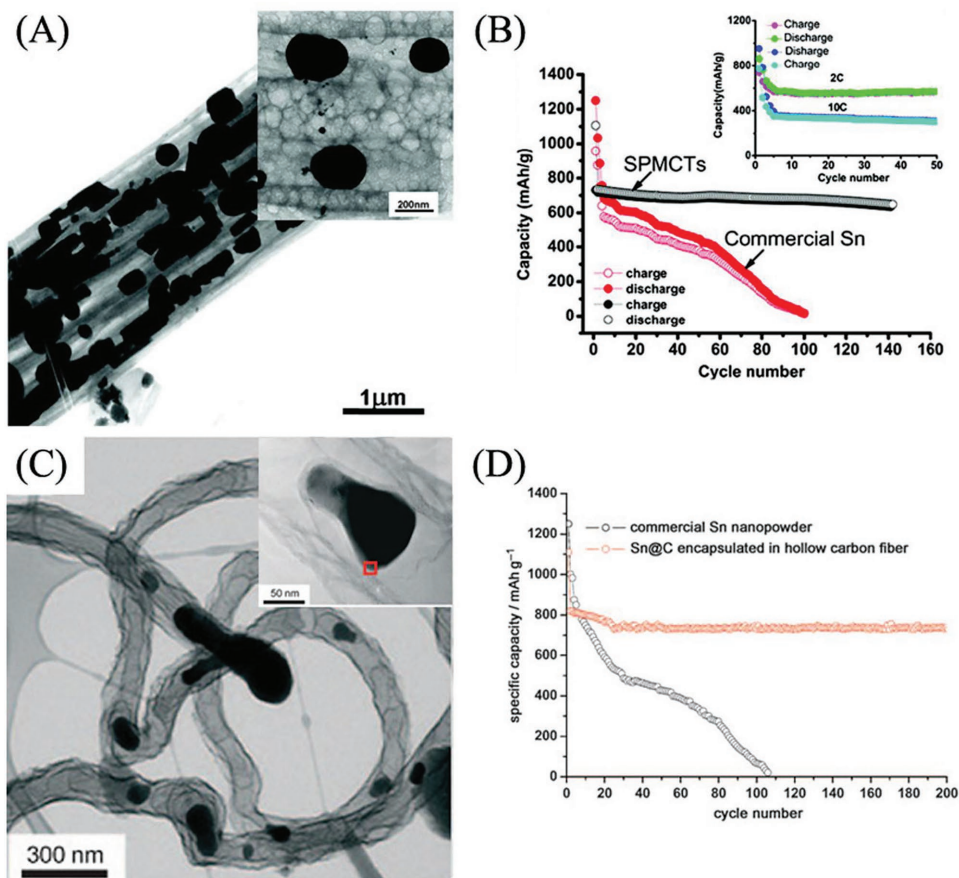


Figure 8. A,B) TEM images (A) and cycle performance (B) of Sn particles encapsulated in porous multichannel carbon microtubes (SPMCTs) at a current density of 0.5C. Reproduced with permission.^[73] Copyright 2009, American Chemical Society. C,D) TEM images (C) and cycle performance (D) of Sn@C encapsulated in hollow carbon fiber. Reproduced with permission.^[74] Copyright 2009, American Chemical Society.

crucial to obtaining excellent capacity retention, as shown in Figure 8B,D.

3.2.2. Nanowires (NWs) and Nanotubes (NTs)

In 2007, Cui's group^[23] reported Si and Ge nanowires (NWs) synthesized by the vapor–liquid–solid (VLS) strategy, which serve as anode materials to obtain improved electrochemical performance for LIBs. As displayed in Figure 9A, NWs experience a volume change without fracture due to the nanosized diameter. Additionally, the abundant empty space between the NWs was able to accommodate the volume expansion of lithiated NWs, maintaining the stability of the entire electrode. Moreover, the NWs were grown directly on stainless-steel current collectors, which enabled robust electrical contact between the NWs and the current collectors to obtain highly efficient 1D electron-transport pathways along the NWs. Figure 9B,D presents the morphology of pristine Si NWs and Ge NWs, respectively. Their diameter ranges from 50 to 100 nm. After several cycles, the volume variation of the NWs and the formation of SEI layers led to an increase of the diameter of the NWs. However, no fracture and pulverization were observed (Figure 9C,E). This structure design resulted in an improved electrochemical

performance at C/20, and the corresponding reversible capacities were about 3100 mA h g⁻¹ and 1100 mA h g⁻¹ for Si NWs and Ge NWs, respectively.

In addition to nanowires, nanotubes are another promising 1D structure suitable for M anode materials. Similar to the result by Cui, Song and co-workers^[77] fabricated silicon nanotube (Si NT) arrays grown on a stainless-steel substrate via combination of the template method and chemical vapor deposition (CVD). As shown in Figure 10A, the prepared Si NT arrays (inner and outer diameter of ≈60 and 120 nm, respectively), vertically aligned on the substrate, displayed a void space between adjacent NTs. Benefiting from the void space inside the nanotubes, as shown in Figure 10C–E, the Si NTs displayed a modest increase in the diameter direction (around 50% from 120 to 180 nm) after lithiation. In addition, they could maintain the overall structure after the first cycle, delivering an enhanced cycle performance (Figure 10B).

3.2.3. Core–Shell NWs or NTs

To further maintain electrical contact between the current collectors and active materials, as well as structural stability during volume variation, the core–shell design is one promising

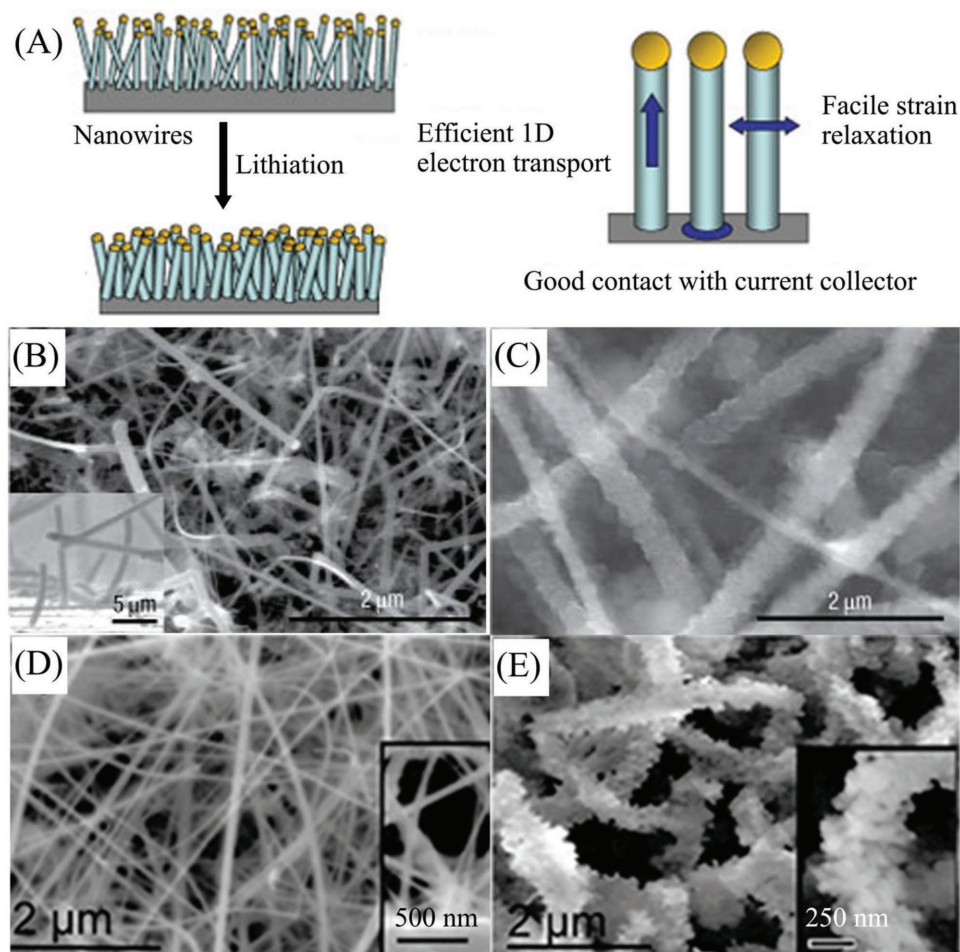


Figure 9. A) Schematic of morphological changes of Si and Ge nanowires during the lithiation process. B,C) SEM images of Si NWs before (B) and after (C) electrochemical cycling. A–C) Reproduced with permission.^[23] Copyright 2007, Nature Publishing Group. D,E) SEM images of Ge NWs before (D) and after (E) electrochemical cycling. D,E) Reproduced with permission.^[23] Copyright 2007, American Chemical Society.

concept that includes two main parts (structurally stable materials as supports and M-based anode materials as electrochemically active materials).^[13] Their combination can form two typical core–shell structures, support (core)–active material (shell) composites and active material (core)–support (shell) composites. In the former electrically conductive materials tend to be selected as the core to enhance the electronic transport, such as, Cu,^[87] carbon nanotubes,^[89] and carbon nanofibers.^[82] Cui and co-workers^[82] presented a novel design of carbon–silicon core–shell nanowires. Commercial carbon nanofibers served as the core while the amorphous silicon worked as the shell. Via the CVD strategy, amorphous silicon was uniformly coated on the carbon nanofibers, and the corresponding diameter increases from 60 nm to 150 nm (Figure 11A,B), indicating a thick silicon coating layer. Since a fully lithiated phase would result in a volume change of $\approx 400\%$, the authors reduced the amount of Li uptake within the Si by limiting the voltage cut-off window to >0.1 V. In addition, the core section of the carbon nanofibers has excellent mechanical stability during cycling, guaranteeing efficient electron transport. Both conscious control in cycling process and the support effect from the carbon

nanofiber make the C–Si core–shell NWs show a large improvement in structural stability and electrochemical performance (Figure 11C,D).

Furthermore, the active material (core)–support (shell) structure is another powerful design, whose shell sections not only provides efficient electron-transport pathways along the shell, but also controls the formation of the SEI layers. Seo et al.^[93] fabricated uniform carbon layers on the surface of Ge NWs (c-Ge-NW) via the CVD strategy, significant to improving the structural stability and electrochemical performance of Ge NWs. Compared with uncoated Ge NWs, the c-Ge-NWs delivered enhanced capacity retention. Besides the electrical conductive materials as the shell section, oxide layers have been also studied as coating layers to stabilize the structure and the SEI layers.^[94–96] Wu and co-workers^[92] designed and prepared a novel double-walled Si–SiO_x nanotube (DWSiNT) anode with an inner wall of active silicon and an outer wall of SiO_x. As shown in Figure 12A, the outer SiO_x layers, which allowed lithium ions to pass through, functioned as mechanical clamping layers. The inner Si layers will expand inward to the hollow space due to the confinement effect of the outer SiO_x

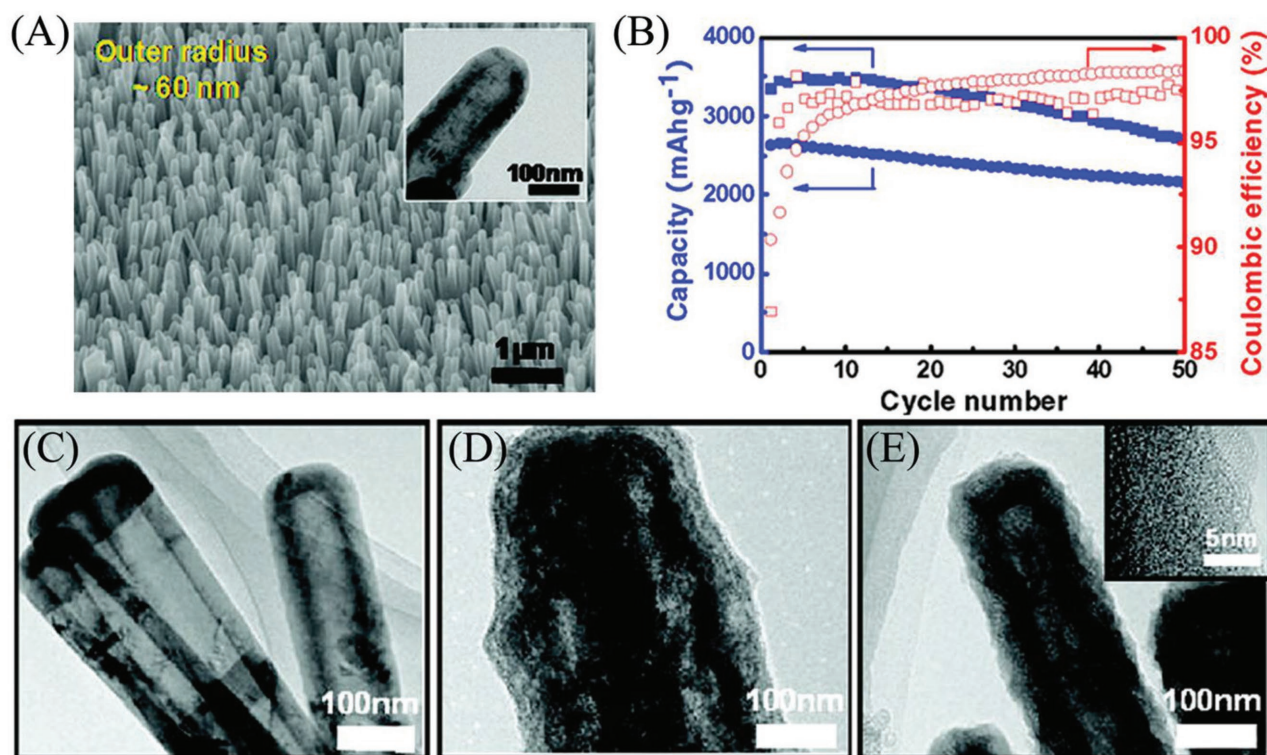


Figure 10. A,B) SEM and TEM images (A) and cycle performance (squares: 0.05C, circles: 0.2C) (B) of Si nanotubes. C–E) Morphological change during the first cycle: TEM images of Si nanotubes at the pristine state (C), the lithiated state (D), and the delithiated state (E). Reproduced with permission.^[77] Copyright 2010, American Chemical Society.

layers, which will also hinder the inner Si layers from contacting with the electrolyte. Because of this structure design, the SEI layers will remain stable without cracking and continuous growth. Figure 12B,C present SEM images of DWS-iNTs before cycling and after a long cycle life of 2000 times; the double-walled nanotubes maintain their pristine structure with very thin SEI layers, consistent with the almost overlapping electrochemical impedance spectroscopy (EIS) curves (Figure 12D). Consequently, the double-layer design realizes excellent capacity retention of 94% and 76% after 500 and 900 cycles, respectively (Figure 12E).

3.3. Two-Dimensional (2D) Structures

Two-dimensional (2D)-structured M anode materials have been explored to improve the electrochemical performance, including two main types of materials, M thin-film materials^[97–99] and M-graphene composite materials.^[100–102] Ohara et al.^[97] presented that thin-film silicon anode materials were able to deliver a high reversible capacity of 3800 mA h g⁻¹. However, the thickness of the silicon thin film was just 50 nm, indicating very low mass loading of the electrodes. To increase the mass loading of the silicon film and enhance the structural stability, simultaneously, Lee and co-workers^[98] fabricated thicker silicon film (diameter of around 300 nm), which was coated with fullerene C60 to form a stable SEI layer. The composite film showed good

electrochemical performance with a specific capacity of above 2000 mA h g⁻¹.

Besides, another widely studied 2D M anode material is M-graphene composites. Graphene is an allotrope of carbon with an atomic-scale honeycomb lattice, displaying high electrical conductivity, large surface area, and excellent chemical and structural stability.^[103–105] These properties make graphene good substrate materials to improve the electrochemical performance of M anode materials. Yuan and co-workers^[102] fabricated one carbon-coated Ge/reduced graphene oxide (Ge/RGO/C) nanocomposite via a facile solution-based strategy. As shown in Figure 13A,B, Ge nanoparticles (diameter: tens of nanometers) were uniformly distributed on the surface of the graphene sheets. Even after cycling 600 times, the Ge/RGO/C nanocomposite retained its pristine structure with homogeneously dispersed Ge nanoparticles on intact graphene sheets (Figure 13C), suggesting excellent cycling performance. Cycled at a current density of 1C, the Ge/RGO/C nanocomposite delivered a high capacity of 993 mA h g⁻¹ after 600 cycles without capacity fading, showing great promise for application in practical full batteries (Figure 13D). Furthermore, graphene is usually chemically functionalized to obtain particular properties for broadened applications, such as nitrogen-doped graphene with tunable activation region and Fermi level.^[106] Zhou and co-workers^[101] presented a SnO₂ nanocrystal/nitrogen-doped reduced graphene oxide (SnO₂NC@N-RGO) nanocomposite, in which SnO₂ nanocrystals were bound on the graphene sheets by Sn–N bonding. As

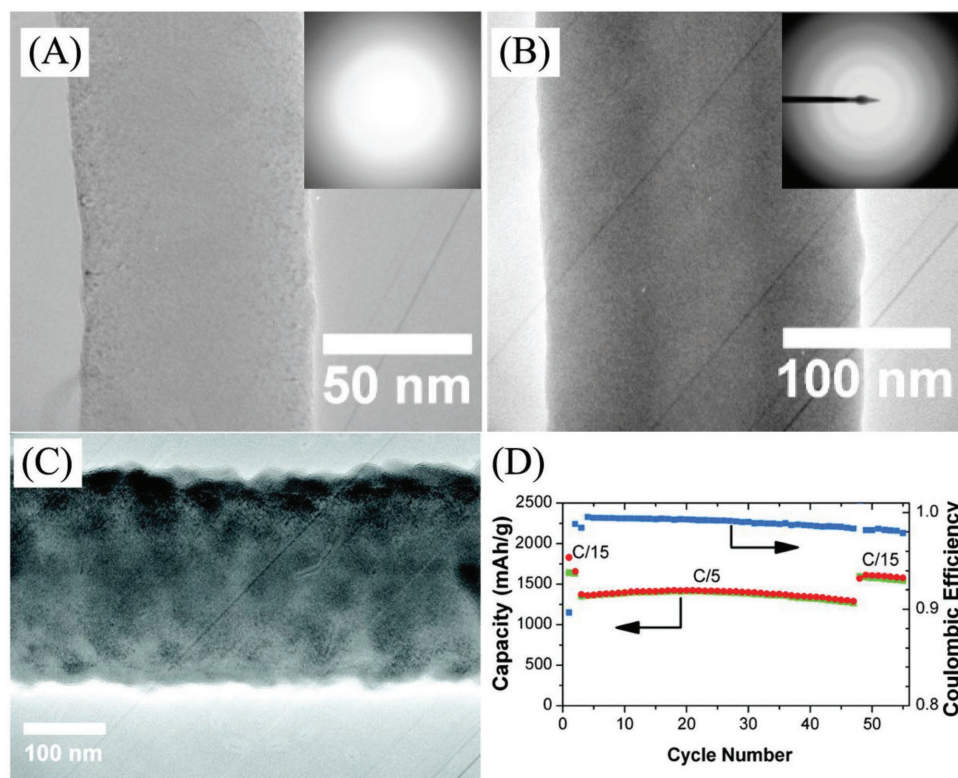


Figure 11. A,B) TEM and selected area electron diffraction (SAED) images of carbon nanofibers (A), C–Si core-shell nanowires (B), and TEM image (C) of C–Si core-shell nanowires cycled after 5 cycles. D) Cycle performance of C–Si core-shell nanowires cycled between 0.1–1 V vs Li/Li⁺. Reproduced with permission.^[82] Copyright 2009, American Chemical Society.

presented in **Figure 14A,B**, the SnO₂NC@N-RGO displayed a typical 2D structure with SnO₂ nanocrystals coated on the surface of the graphene sheets. The Sn–N bonding between the SnO₂ nanocrystals and the N-RGO was confirmed by X-ray absorption near edge structure (XANES) measurements. The C K-edge peak intensity of the SnO₂NC@N-RGO is higher than that of N-RGO, indicating possible formation of bonding between the carbon atoms in the graphene between the nitrogen and oxygen species, corresponding to an obvious decrease of Sn L₃-edge peak intensity. (Figure 14C,D). The particular binding structure led to an excellent cycle performance for the obtained composites. They displayed a high reversible capacity of 1346 mA h g⁻¹ after 500 cycles at 0.5 A g⁻¹ (Figure 14 E).

3.4. Three-Dimensional (3D) Structures

Compared with the above three types of structures discussed (i.e., 0D, 1D, and 2D structures), the three-dimensional (3D) structures can provide highly efficient electronic conductive networks for active materials to enhance the electrochemical activity of anode materials. Recently, 3D M anode materials have attracted intense attention. Two main strategies have been developed to fabricate the 3D structures, such as 3D porous M materials and M nanomaterials with 3D porous substrates. Benefiting from the 3D structures, the as-prepared

3D M anode materials show improved electrochemical performance.

3.4.1. 3D Porous M Materials

The fabrication of 3D porous M materials can be divided to two strategies, including top-down and bottom-up methods. Generally, the top-down method employs bulk-sized M-based materials as the starting precursors to prepare 3D porous structures by electroless or electrochemical etching techniques.^[27,107–111] By controlling the etching processes, the obtained porous structures can be tuned to realize appropriate pore size and porosity. Different from the top-down strategy, the bottom-up method usually utilizes porous templates to deposit M-based materials to firstly form composites. After removal of the templates, corresponding voids (e.g., channels or pores) will be obtained in the resulting materials, finally forming the 3D porous M materials. The templates and the deposition procedure are the key to controlling the structures of the obtained M materials.

Bang and co-workers^[107] applied the metal-assisted chemical-etching method to prepare a carbon-coated 3D macroporous-Si anode material. Specifically, bulk-sized Si particles were firstly deposited with Ag nanoparticles, which were then chemically etched in HF/H₂O₂. During the process, the sections of the bulk-sized Si deposited with the Ag nanoparticles would

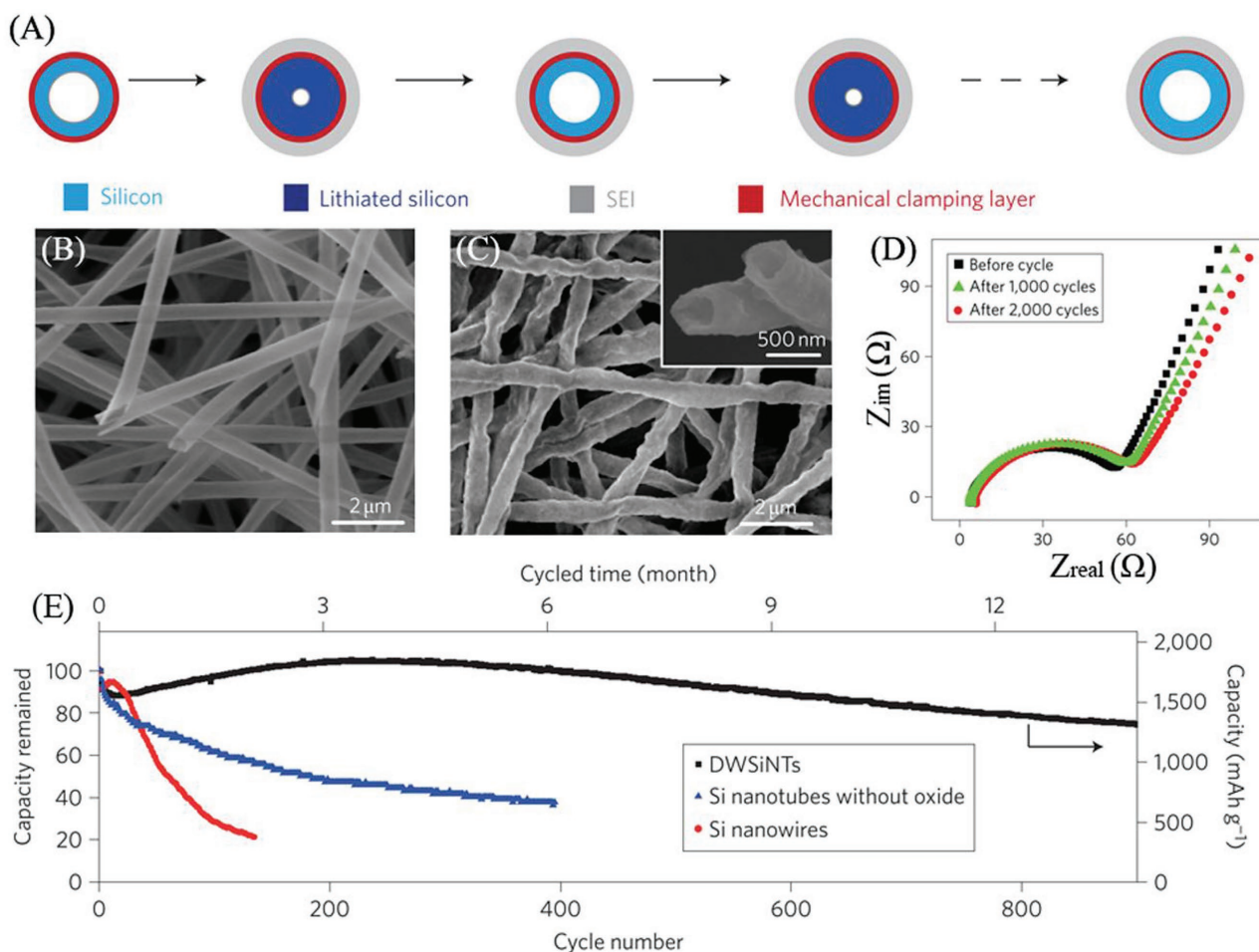


Figure 12. A–C) Schematic showing SEI formation (A) and SEM images of the double-walled Si–SiO_x nanotube (DWSiNT) before cycling (B) and after 2000 cycles (C). D, E) Impedance measurements for DWSiNT after different numbers of cycles (D) and cycle performance of DWSiNT and other two Si anode materials (i.e., Si nanotubes without SiO_x layers and Si nanowires) (E). Reproduced with permission.^[92] Copyright 2012, Nature Publishing Group.

undergo one electrochemical reaction with Ag and Si as cathode and anode, respectively. By this means, the Si below the Ag nanoparticles could form soluble $[\text{SiF}_6]^{2-}$ and be continuously etched to make 3D macroporous structures. After the CVD process, the carbon-coated 3D macroporous-Si anode material was obtained. **Figure 15A** shows the morphology of these materials. The macroporous structure and uniform carbon-coating layers are beneficial to ensure the structural stability during cycling (**Figure 15B**). Owing to the efficient electrolyte infiltration and conductive networks of the stable 3D macroporous structures, these Si–C materials present improved capacity retention of 87% after 50 cycles at 0.2C and excellent rate performance (**Figure 15C,D**). This strategy realized this metal-assisted etching process in a single material by introducing Ag nanoparticles via the electrodeless metal deposition. Different from this strategy, other methods utilize composite materials, in which one or several substances are dissolved in the etching solution, while others would be left to form the porous materials. Among these strategies, magnesiothermic reduction has been widely applied to form 3D porous-Si anode materials.^[111]

During the magnesiothermic reduction, the starting materials, usually SiO₂, can be partially reduced to Si, forming a composite of Si and MgO. After removing MgO by using an acid solution, the 3D porous-Si materials can be prepared. Liu et al.^[27] employed 3D porous SiO₂ converted from natural reed leaves as the precursors, fabricating one 3D highly porous Si–C hierarchical architecture via the magnesiothermic reduction and the carbon-coating process. The reed leaves firstly went through a thermal treatment to get rid of their organic matter and forming a 3D porous SiO₂ skeleton. After the magnesiothermic reduction, the generated MgO functioned as a pore template to increase the porosity after treatment with HCl. After the carbon-coating process, the desired 3D porous Si–C was finally obtained. **Figure 16A** shows the SEM images of the obtained 3D hierarchically porous structures, consisting of highly porous 2D nanosheets/nanonets. High-resolution TEM (HRTEM) imaging confirmed the uniform carbon layers coated on the surface of the 3D porous Si (**Figure 16B**). This novel structure was capable of buffering the huge volume change and facilitating the transport of electrons and ions, presenting

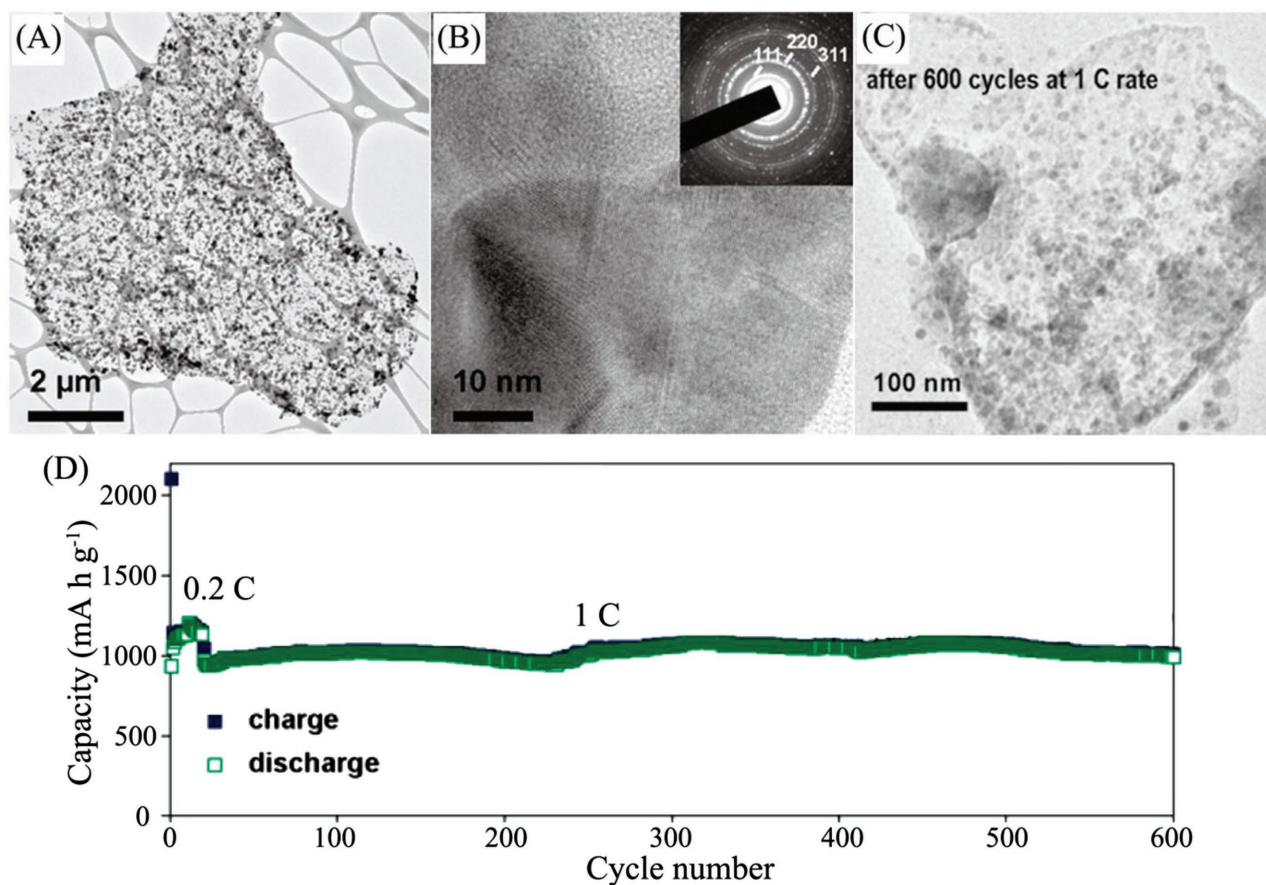


Figure 13. A,B) TEM (A) and HRTEM and SAED images (B) of the carbon-coated Ge/RGO (Ge/RGO/C) nanocomposite. C) TEM image of the Ge/RGO/C nanocomposite after 600 cycles. D) Cycle performance of the the Ge/RGO/C nanocomposite at a current density of 1C, firstly cycled at 0.2C for 15 cycles. Reproduced with permission.^[102] Copyright 2014, American Chemical Society.

a long-term cycle performance of around 420 mA h g⁻¹ after 4000 cycles (Figure 16C).

On the other hand, the bottom-up strategy is another promising method to prepare 3D porous M anode materials via template-based strategies.^[26,112–114] Yao and co-workers^[113] used silica nanospheres as the template to fabricate an electrode made of interconnected hollow Si nanospheres, as shown in Figure 17A. The silica particles of a uniform diameter of 350 nm were firstly drop-coated on a stainless-steel substrate, which was subsequently deposited with amorphous Si layers via the CVD process. Then, the silica template was removed by HF etching, forming the interconnected hollow Si nanospheres. Figure 17B shows the morphology of the prepared electrode with interconnected hollow Si nanospheres of an inner diameter of ≈350 nm and an outer diameter of ≈400 nm). Similar to the hollow-nanoparticle electrodes discussed in Section 3.1, the fabricated electrode showed excellent structural stability after 700 cycles because the porous structure buffers the huge volume variation of Si during cycling (Figure 17C). The electrode showed a cycling performance at 0.5C with a capacity degradation of 8% per 100 cycles over the total 700 cycles, which should be able to be improved further. Nevertheless, the electrode displayed excellent rate capacities of 2417, 2378, 2060,

1756, and 1387 mA h g⁻¹ at 0.2, 1, 2, 5, and 10 C, respectively, owing to the interconnected porous structure.

3.4.2. M Nanomaterials with 3D Porous Substrates

Numerous 3D porous substrates, usually electronic conductive, have been widely utilized to fabricate M anode composites, such as porous metals,^[115] porous carbon,^[116,117] carbon nanotubes,^[118,119] graphene,^[120–125] and conductive polymers.^[126] Among them, 3D porous metal substrates can be easily prepared via the etching strategy discussed above in Section 3.4.1. Yu and co-workers^[115] presented a 3D bicontinuous Au/amorphous Ge (Au/a-Ge) electrode by employing a 3D nanoporous Au film as the substrate. The nanoporous Au film (thickness: ≈100 nm) was firstly prepared via the chemical etching of Ag₆₅Au₃₅ alloy leaves through a HNO₃ aqueous solution, forming the 3D nanoporous structure (Figure 18A). Next, the nanoporous Au films were deposited with amorphous Ge layers (thickness: ≈20 nm) by thermal evaporation, to form the 3D porous bicontinuous Au/a-Ge electrode (insert in Figure 18A). Owing to the robust structural stability of the amorphous Ge and enough void space around the Ge layers on cycling, the electrode retained the 3D

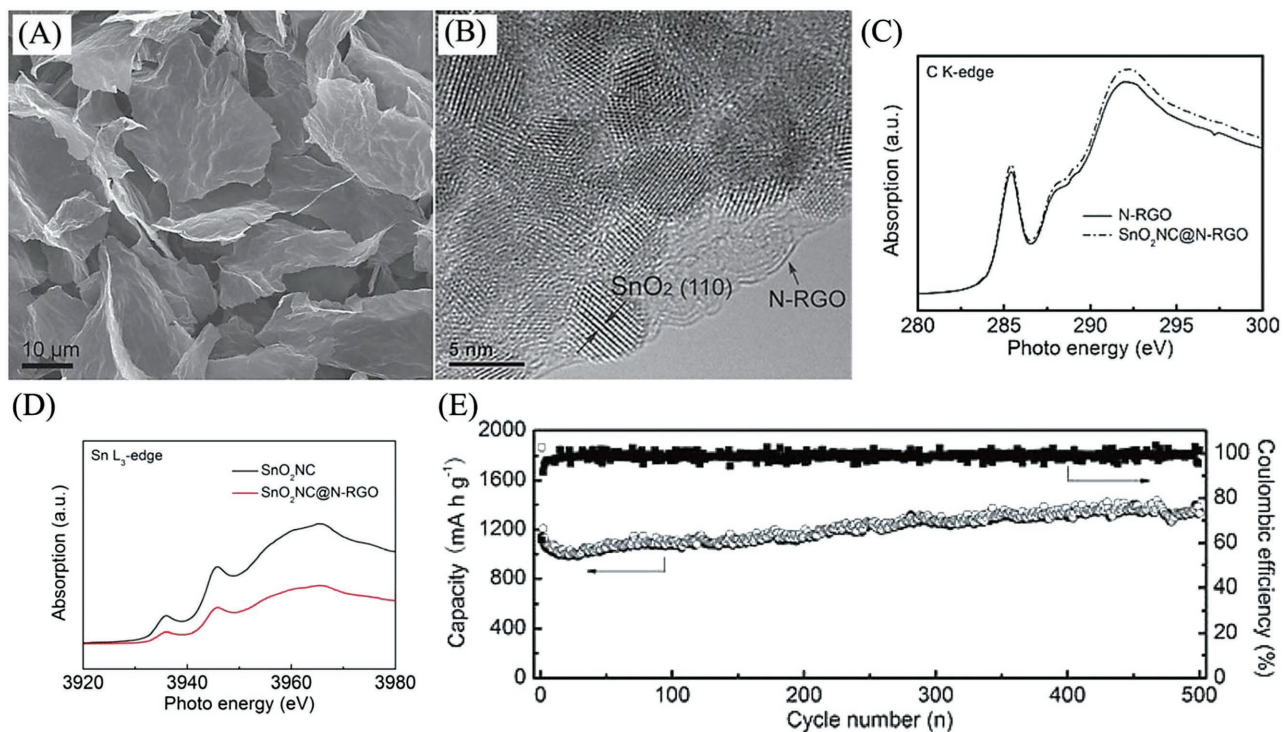


Figure 14. A,B) SEM (A) and TEM (B) images of the SnO₂ nanocrystal/nitrogen-doped reduced graphene oxide hybrid material (SnO₂NC@N-RGO). C,D) C K-edge (C) and Sn L₃-edge (D) XANES of N-RGO and SnO₂NC@N-RGO. E) Cycle performance and Coulombic efficiency of the SnO₂NC@N-RGO cycled at a current density of 0.5 A g⁻¹. Reproduced with permission.^[101] Copyright 2013, Wiley-VCH.

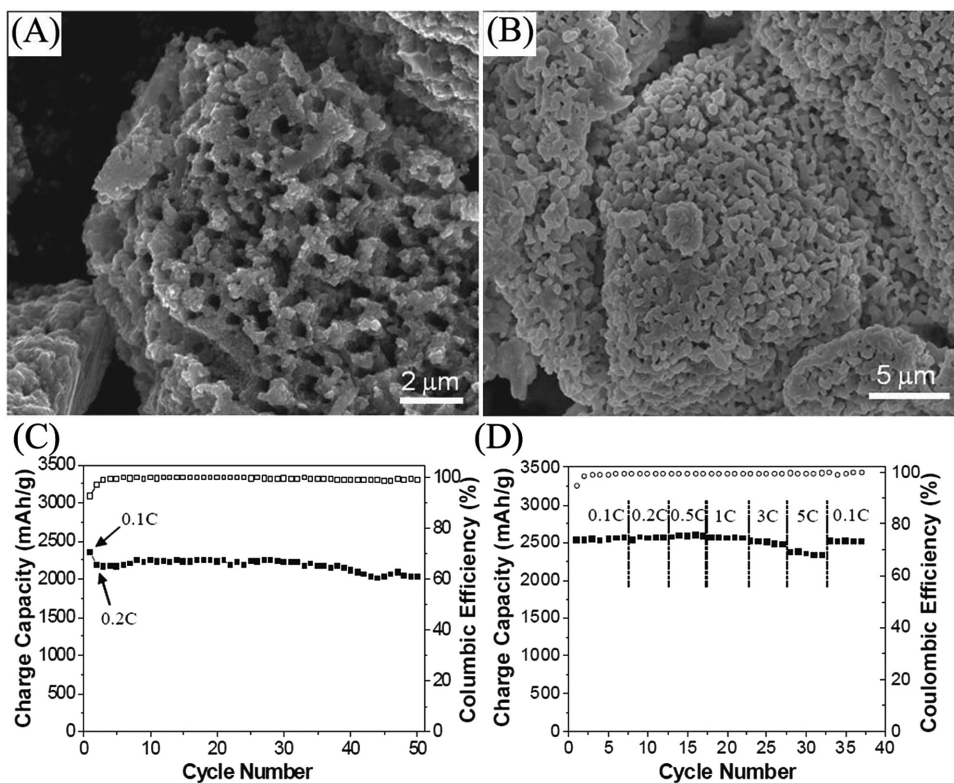


Figure 15. A,B) SEM images of the carbon-coated 3D macroporous Si anode materials before (A) and after (B) electrochemical cycles. C,D) Cycle performance (C) and rate capability (D) of the carbon-coated 3D macroporous Si anodes. Reproduced with permission.^[107] Copyright 2012, Wiley-VCH.

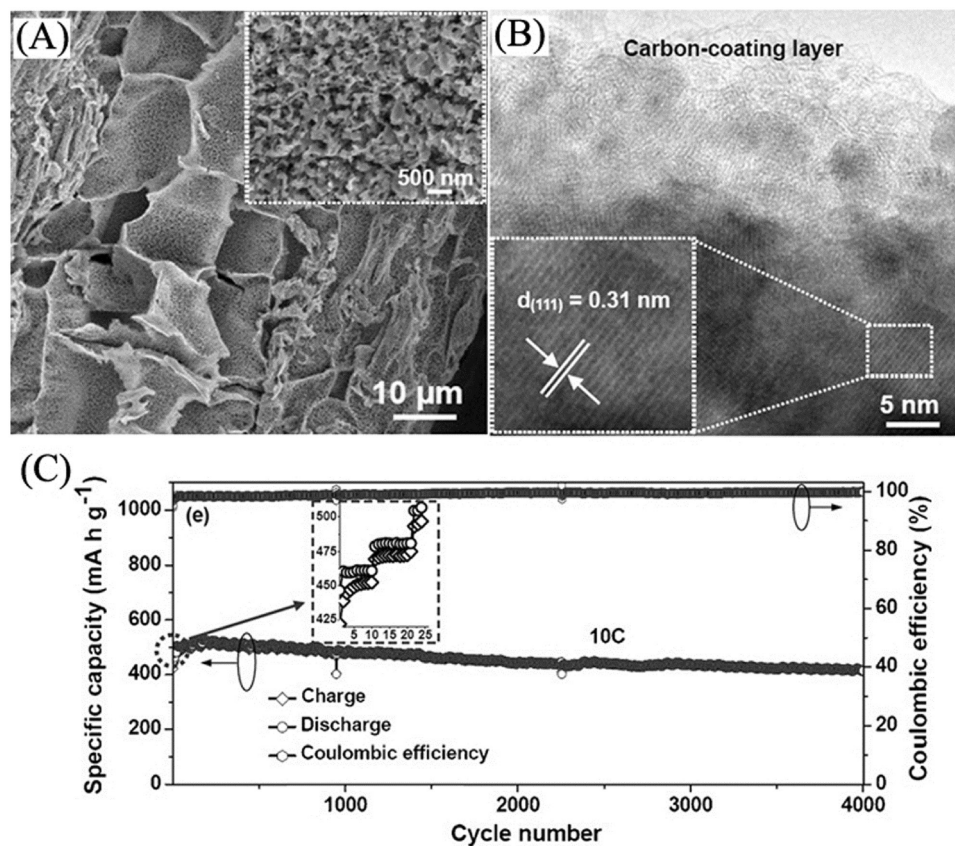


Figure 16. A,B) SEM (A) and HRTEM (B) images of the 3D highly porous SiC hierarchical architectures. C) Cycle performance of 3D highly porous SiC anode materials. Reproduced with permission.^[27] Copyright 2015, Wiley-VCH.

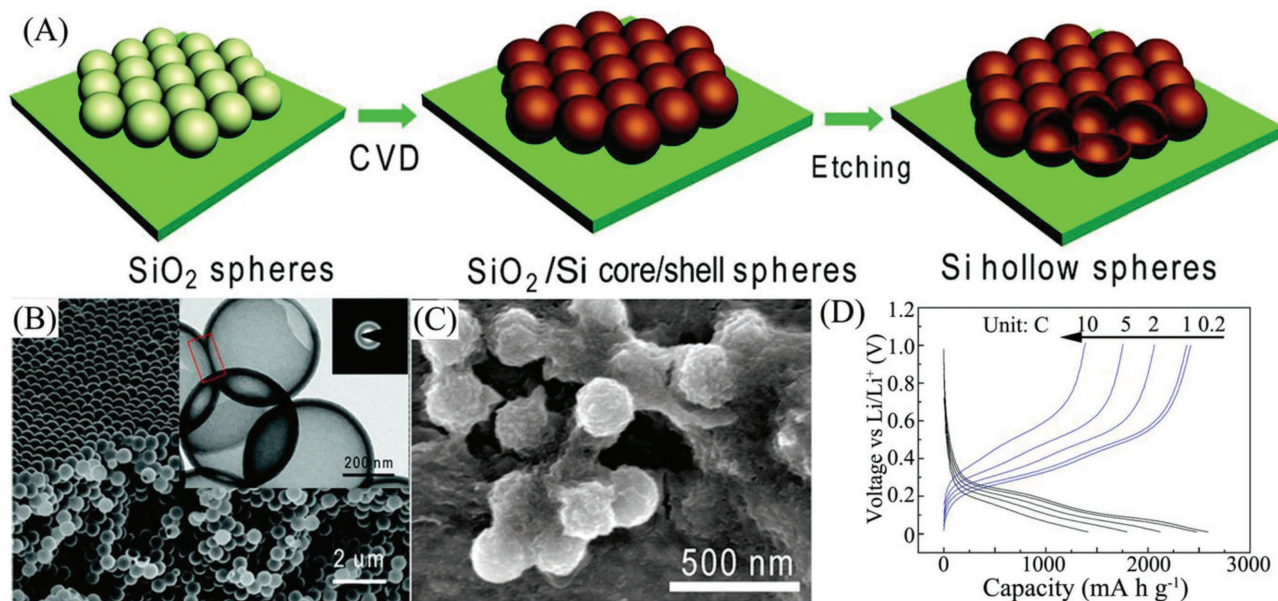


Figure 17. A,B) Schematic of the preparation process (A) and SEM and TEM images (B) of the interconnected Si hollow nanosphere electrode. C) SEM image of the electrode after 700 cycles. D) Rate performance of the electrode. Reproduced with permission.^[13] Copyright 2011, American Chemical Society.

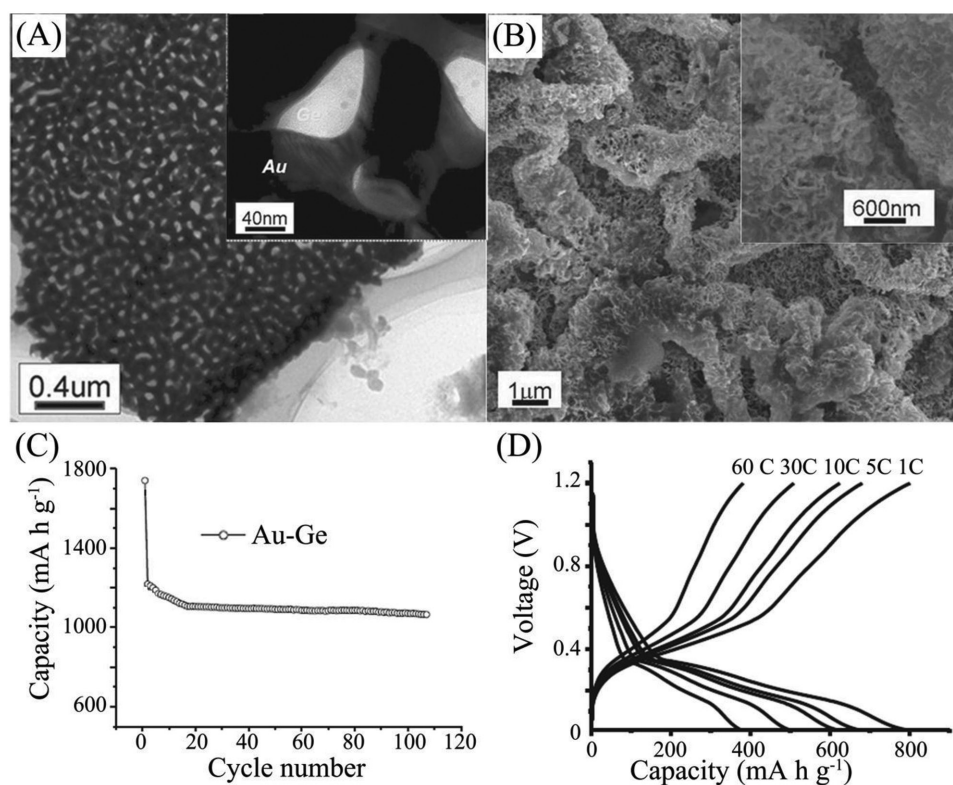


Figure 18. A) TEM image of the as-prepared 3D nanoporous Au; the inset shows a TEM image of the 3D bicontinuous Au/a-Ge composite. B) SEM image of the electrode after 100 cycles at 0.2C. C,D) Cycle performance at 0.2C (C) and voltage profiles at various current densities (1, 5, 10, 30, and 60C) (D) of the electrode. Reproduced with permission.^[115] Copyright 2012, Wiley-VCH.

bicontinuous porous structure without separation of the a-Ge and the Au substrate (Figure 18B). Due to the excellent structural stability, as shown in Figure 18C, the electrode showed an enhanced capacity retention of 87.5% with a high reversible capacity of around 1066 mA h g^{-1} after 100 cycles at 0.2C. More importantly, the 3D porous Au substrate and the bicontinuous porous electrode provide pathways for highly rapid transfer of electrons and ions along the conductive network and the pore network, simultaneously. As shown in Figure 18D, the electrode presented superior rate capacities of 800, 680, 625, 505, and 380 mA h g^{-1} at 1, 5, 10, 30, and 60C, respectively.

As discussed above, graphene is one promising carbon-based substrate to prepare 2D graphene-M anode materials to improve the electrochemical performance. Compared with 2D graphene sheets, 3D graphene networks have attracted increasing attention due to their unique physicochemical properties.^[127] Focusing on Sn-based anode materials, Wu and co-workers^[122] designed and prepared a 3D nanoarchitecture with Sn-based nanoparticles encapsulated in a 3D porous graphene network (pGN) via a surfactant-assisted assembly method. As displayed in Figure 19A, a large number of vacancies were generated by using polystyrene nanospheres as templates, which could be decomposed under thermal treatment. In addition, through tuning the atmosphere during the annealing of the precursors for the Sn-based nanoparticles, two kinds of anode materials were prepared. The CoSnO_3 nanoparticles encapsulated in pGN (0D-CoSnO₃@3D-pGN) and Co-Sn

nanoparticles encapsulated in pGN (0D-Co-Sn@3D-pGN) show similar structures (Figure 19B,C). Owing to the 3D porous conductive graphene network, nanoscale electroactive particles and void-space design, both Sn-based materials presented improved capacity retention and excellent rate performance (Figure 19D,E).

4. Conclusions and Perspective

Here, we have briefly summarized the recent progress of Si-, Ge-, and Sn-based anode materials for LIBs. Owing to their high theoretical capacities, these three alloy-type anode materials have attracted intense attention as anode materials, as candidates for next-generation LIBs. However, there are still significant barriers that need to be solved, such as the huge volume change during the lithiation/delithiation processes, the cracking and pulverization of the anode materials and overall electrodes, and the unstable SEI layers. To overcome these challenges, a series of novel nanostructures has been designed and constructed. We have classified these structures as four types, zero-, one-, two-, and three-dimensional nanostructures, focusing on dimensional control on structure design, as shown in Table 2–5. There are similarities among these four types of structures, like hollow structures, core-shell architectures, and void-space design. Nevertheless, there are also several obvious differences in comparing these structures. As the structure

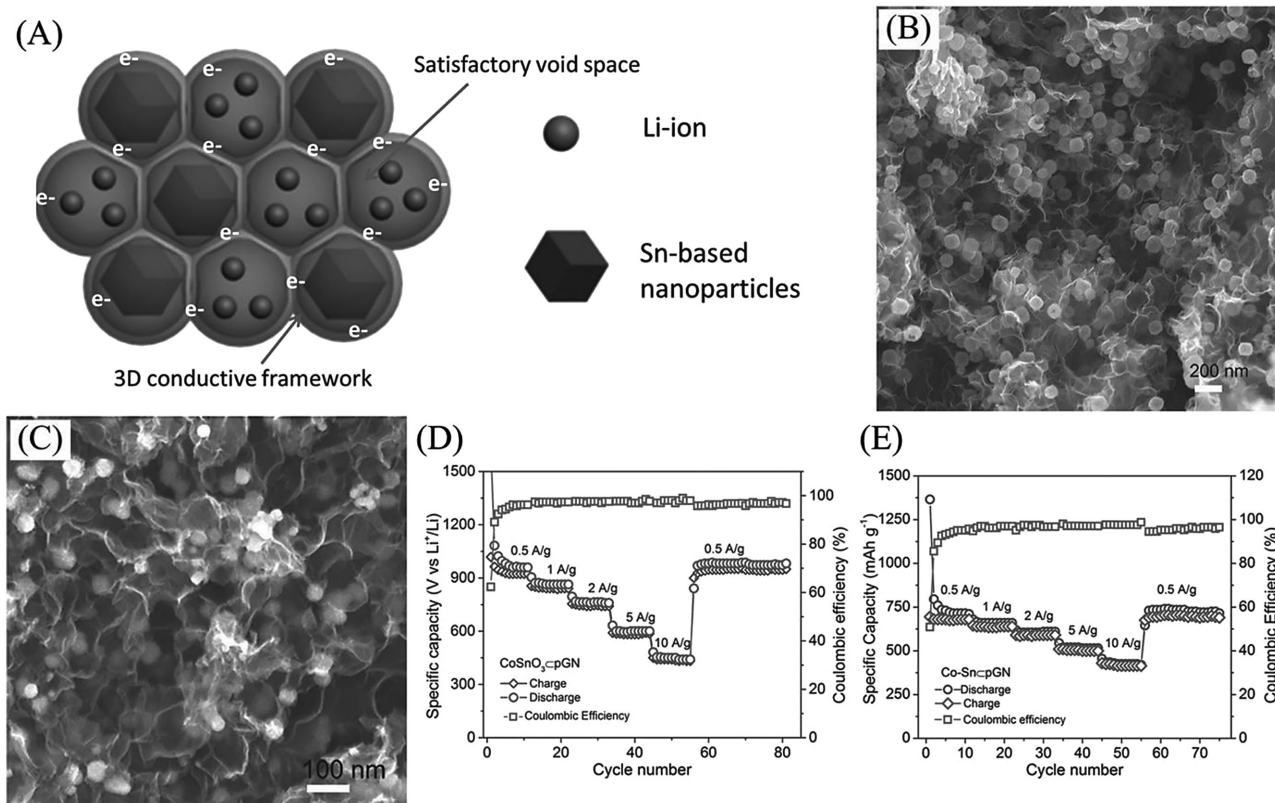


Figure 19. A) Schematic of the 3D porous graphene network encapsulating Sn-based nanoparticles. TEM images of CoSnO_3 nanoparticles encapsulated in 3D porous graphene network (0D- CoSnO_3 @3D-pGN) (B) and Co-Sn nanoparticles encapsulated 3D porous graphene network (0D-Co-Sn@3D-pGN) (C). D,E) Rate performance of 0D- CoSnO_3 @3D-pGN (D) and 0D-Co-Sn@3D-pGN (E). Reproduced with permission.^[122] Copyright 2015, Wiley-VCH.

design will result in different particle sizes and protection layers of M anode materials, the cyclability will be affected by the structure. In addition, the electronic and ionic conductivity of the structures with different dimension-design will be different. 0D nanoparticles will build transport pathways of electrons and ions along with the additives (i.e., binders, conductive additives, and current collectors) in the prepared electrodes. Another three types of structures will also provide different electronic and ionic pathways along the structure. The difference between particle size and electronic/ionic conductivity

will be the crucial factor to improve the electrochemical performance of M anode materials. Moreover, the unique properties of these nanostructures make the electrodes show different configurations, such as free-standing and flexible electrodes. Via the fabrication of nanosized structures with rational design, these M-based anode materials exhibit excellent structural stability and capacity retention. In addition, these nanostructures provide highly efficient transport pathways for ions and electrons, which is critical to significantly improve the rate performance. This reasonable structural design is necessary to

Table 2. Electrochemical performance of 0D nanomaterials designed for M anode materials.

Materials	Structure	Electrochemical performance	Rate
$\text{Si}^{[59]}$	Nanoparticles	1180 mA h g^{-1} after 500 cycles	3 A g^{-1}
$\text{Sn-C}^{[60]}$	Nano-Sn/C composite nanoparticle	710 mA h g^{-1} after 120 cycles	0.2 A g^{-1}
$\text{Ge-C}^{[61]}$	Composite nanoparticles	$\approx 700 \text{ mA h g}^{-1}$ after 50 cycles	0.15 A g^{-1}
$\text{Sn-Ni}^{[64]}$	Porous Ni-Sn Microcages	534 mA h g^{-1} after 1000 cycles	1C
$\text{Si-Cu}^{[65]}$	Cu-coated Si nanoparticles	$\approx 570 \text{ mA h g}^{-1}$ after 20 cycles	0.07 A g^{-1}
$\text{Si-Ag}^{[63]}$	Ag-coated hollow porous Si nanoparticles	$\approx 3000 \text{ mA h g}^{-1}$ after 100 cycles	0.5 A g^{-1}
$\text{Si-SiO}_x\text{-C}^{[67]}$	SiO_x/C -coated Si nanoparticles	$\approx 1100 \text{ mA h g}^{-1}$ after 60 cycles	0.15 A g^{-1}
$\text{Sn-C}^{[30]}$	Sn nanoparticles encapsulated in elastic hollow C spheres	$\approx 550 \text{ mA h g}^{-1}$ after 100 cycles	0.2C
$\text{Si-C}^{[68]}$	Nonfilling carbon-coated porous Si microparticles (core-shell)	1490 mA h g^{-1} after 1000 cycles	0.25C

Table 3. Electrochemical performance of 1D nanomaterials designed for M anode materials.

Materials	Structure	Electrochemical performance	Rate
Si-C ^[72]	Si nanoparticles embedded in carbon nanofibers	721 mA h g ⁻¹ after 300 cycles	3C
Si-C-TiO _{2-x} ^[70]	Si nanoparticles embedded in TiO _{2-x} /C porous microfibers	1134 mA h g ⁻¹ after 50 cycles	0.2C
Ge-C ^[24]	Ge nanoparticles embedded in carbon nanowires	1200 mA h g ⁻¹ after 50 cycles	0.2C
Sn-C ^[74]	Sn@carbon nanoparticles embedded in bamboo-like hollow carbon nanofibers	737 mA h g ⁻¹ after 200 cycles	0.1C
Sn-C ^[73]	Sn nanoparticles embedded in porous multichannel carbon microtubes	648 mA h g ⁻¹ after 140 cycles	0.5C
Si ^[23]	Si nanowires	3200 mA h g ⁻¹ after 10 cycles	0.05C
Ge ^[81]	Ge nanowires	≈1000 mA h g ⁻¹ after 20 cycles	0.05C
Si ^[77]	Arrays of sealed Si nanotubes	≈2750 mA h g ⁻¹ after 50 cycles	0.05C
Si ^[78]	Porous boron-doped Si nanowires	≈1000 mA h g ⁻¹ after 2000 cycles	1C
Si ^[76]	Si nanotubes	≈3000 mA h g ⁻¹ after 80 cycles	1C
Si ^[79]	Si nanowires	≈1500 mA h g ⁻¹ after 30 cycles	0.2C
Si ^[90]	Crystalline-amorphous core-shell Si nanowires	≈1060 mA h g ⁻¹ after 100 cycles	0.2C
Si-C ^[82]	Carbon-coated Si nanowires	≈1800 mA h g ⁻¹ after 55 cycles	0.2C
Si-C ^[85]	Carbon coated Si nanowires	≈2000 mA h g ⁻¹ after 55 cycles	0.1C
Si-polymer ^[91]	PEDOT coated Si nanowires	2510 mA h g ⁻¹ after 100 cycles	0.2C
Ge-C ^[93]	Carbon-coated Ge nanowires	≈700 mA h g ⁻¹ after 55 cycles	0.5C
Ge-C ^[83]	Graphene-coated Ge nanowires	≈1059 mA h g ⁻¹ after 200 cycles	4C
Si-SiO _x ^[92]	Double-walled Si-SiO _x nanotube	≈1300 mA h g ⁻¹ after 900 cycles	0.2C
Ge-C ^[84]	Ge nanowires embedded in graphite nanotubes	≈1200 mA h g ⁻¹ after 100 cycles	0.25 A g ⁻¹
Ge-C ^[88]	Carbon-coated Ge nanotubes	≈900 mA h g ⁻¹ after 50 cycles	0.2C
Ge-Cu ^[87]	Cu-Ge core-shell nanowires	1419 mA h g ⁻¹ after 40 cycles	0.5C
Ge-CNTs ^[89]	CNT-supported Ge nanowires	1314 mA h g ⁻¹ after 100 cycles	0.2C

obtain high-performance M-anode electrode materials, and can be extended to other electrode materials with a huge volume variation, such as other alloy-type and conversion-type electrode materials.

The Si-, Ge-, and Sn-based anode materials show improved electrochemical performance and great promise for application in next-generation LIBs through reasonable nanostructure design. However, there are still several issues that should be overcome in future research. Firstly, the formation of SEI layers on the surface of M-based anode materials should further be defined to obtain high Coulombic efficiency. Secondly, ex situ and in situ characterization strategies need to be introduced to further study the principle of cracking and pulverization of M-based anodes and overall prepared electrodes,

and understand the microscopic processes during cycling. Thirdly, the development of suitable binders and electrolytes for the M-based anodes is essential to further improve the electrochemical performance. Finally, industry-grade preparation of M-based anode materials is urgently required to promote the practical applications of commercial LIBs. For the lithium-ion-battery industry, traditional prepared electrodes consist of 0D microparticle-like electrode materials. To further improve the electrochemical performance of industry-grade electrodes, the structure design of M-based anode materials shows great potential in improving the cyclability and electronic/ionic conductivity. The development of M-based anode materials will provide promising strategies to realize next-generation high-energy lithium-ion batteries.

Table 4. Electrochemical performance of 2D nanomaterials designed for M anode materials.

Materials	Structure	Electrochemical performance	Rate
Si ^[99]	Si thin films	3498 mA h g ⁻¹ after 500 cycles	0.25C
Si-C ^[98]	Fullerene-C60-coated Si thin films	2000 mA h g ⁻¹ after 50 cycles	500 A cm ⁻²
SnO ₂ -C ^[101]	SnO ₂ nanocrystals/N-doped graphene	1346 mA h g ⁻¹ after 500 cycles	0.5 A g ⁻¹
Ge-C ^[102]	Ge nanoparticles loaded on graphene	1166 mA h g ⁻¹ after 75 cycles	0.2C
Ge-C ^[100]	Sandwich-structured C/Ge/graphene nanocomposite	993 mA h g ⁻¹ after 160 cycles	1C (charge) and 0.4C (discharge)

Table 5. Electrochemical performance of 3D nanomaterials designed for M anode materials.

Materials	Structure	Electrochemical performance	Rate
Si ^[113]	3D interconnected hollow Si nanospheres	1420 mA h g ⁻¹ after 700 cycles	0.5C
Ge ^[109]	3D nanoporous Ge	1191 mA h g ⁻¹ after 160 cycles	0.16 A g ⁻¹
Ge ^[112]	3D ordered porous Ge	≈800 mA h g ⁻¹ after 50 cycles	0.2C
Ge ^[26]	3D porous Ge nanoparticles	1415 mA h g ⁻¹ after 50 cycles	1C
Si-C ^[108]	Carbon-coated 3D porous Si	≈1700 mA h g ⁻¹ after 70 cycles	0.2C
Si-C ^[27]	Carbon coated 3D porous Si	420 mA h g ⁻¹ after 4000 cycles	10C
Si-C ^[110]	Carbon-coated interconnected porous Si	1037 mA h g ⁻¹ after 100 cycles	0.05 A g ⁻¹
Si-Ag ^[111]	Ag-coated 3D macroporous Si	1163 mA h g ⁻¹ after 100 cycles	0.2C
Ge-C ^[118]	Ge supported on 3D single-walled carbon nanotubes matrix	417 mA h g ⁻¹ after 40 cycles	0.025 A g ⁻¹
Si-C ^[116]	Carbon-coated Si pomegranates	1160 mA h g ⁻¹ after 1000 cycles	0.5C
Sn-C ^[120]	Sn nanoparticles loaded on interconnected 3D porous graphene networks	682 mA h g ⁻¹ after 1000 cycles	2 A g ⁻¹
Si-C ^[117]	Si nanoparticles loaded on 3D porous carbon black	1590 mA h g ⁻¹ after 100 cycles	1C
SnO ₂ -C ^[124]	Amorphous SnO ₂ loaded on 3D porous graphene nanosheets	793 mA h g ⁻¹ after 150 cycles	0.1 A g ⁻¹
Si-PANI ^[126]	3D porous Si nanoparticles-PANI composite	1600 mA h g ⁻¹ after 1000 cycles	1 A g ⁻¹
CoSnO ₃ -C ^[122]	CoSnO ₃ nanoparticles encapsulated in 3D porous graphene	566 mA h g ⁻¹ after 1500 cycles	2 A g ⁻¹
Ge-Au ^[115]	Amorphous Ge supported on 3D porous Au matrix	1066 mA h g ⁻¹ after 100 cycles	0.2C

Acknowledgements

This work was financially supported by the National Key Research Program (No.2016YFB0100305), the National Natural Science Foundation of China (No. 21373195, 51622210), the "Recruitment Program of Global Experts", the Fundamental Research Funds for the Central Universities (WK3430000004), and the Collaborative Innovation Center of Suzhou Nano Science and Technology.

Received: November 16, 2016
Published online:

- [1] M. I. Hoffert, K. Caldeira, G. Benford, D. R. Criswell, C. Green, H. Herzog, A. K. Jain, H. S. Khesghi, K. S. Lackner, J. S. Lewis, *Science* **2002**, 298, 981.
- [2] A. Midilli, I. Dincer, M. Ay, *Energy Policy* **2006**, 34, 3623.
- [3] G. J. Herbert, S. Iniyar, E. Sreevalsan, S. Rajapandian, *Renewable Sustainable Energy Rev.* **2007**, 11, 1117.
- [4] K. Solangi, M. Islam, R. Saidur, N. Rahim, H. Fayaz, *Renewable Sustainable Energy Rev.* **2011**, 15, 2149.
- [5] M. M. Thackeray, C. Wolverton, E. D. Isaacs, *Energy Environ. Sci.* **2012**, 5, 7854.
- [6] B. Dunn, H. Kamath, J.-M. Tarascon, *Science* **2011**, 334, 928.
- [7] J. Liu, J. G. Zhang, Z. Yang, J. P. Lemmon, C. Imhoff, G. L. Graff, L. Li, J. Hu, C. Wang, J. Xiao, *Adv. Funct. Mater.* **2013**, 23, 929.
- [8] X. L. Wu, Y. G. Guo, L. J. Wan, *Chem.-Asian J.* **2013**, 8, 1948.
- [9] J. B. Goodenough, K.-S. Park, *J. Am. Chem. Soc.* **2013**, 135, 1167.
- [10] P. G. Bruce, B. Scrosati, J. M. Tarascon, *Angew. Chem., Int. Ed.* **2008**, 47, 2930.
- [11] R. Marom, S. F. Amalraj, N. Leifer, D. Jacob, D. Aurbach, *J. Mater. Chem.* **2011**, 21, 9938.
- [12] H.-C. Yu, C. Ling, J. Bhattacharya, J. C. Thomas, K. Thornton, A. Van der Ven, *Energy Environ. Sci.* **2014**, 7, 1760.
- [13] H. Wu, Y. Cui, *Nano Today* **2012**, 7, 414.
- [14] J. B. Goodenough, *Acc. Chem. Res.* **2012**, 46, 1053.
- [15] L. Weihang, Z. Linchao, W. Ying, Y. Yan, *Sci. China Mater.* **2016**, 59, 287.
- [16] B. Diouf, R. Pode, *Renewable Energy* **2015**, 76, 375.
- [17] B. Scrosati, J. Garche, *J. Power Sources* **2010**, 195, 2419.
- [18] Q. Zhang, E. Uchaker, S. L. Candelaria, G. Cao, *Chem. Soc. Rev.* **2013**, 42, 3127.
- [19] Z. Shu, R. McMillan, J. Murray, *J. Electrochem. Soc.* **1993**, 140, 922.
- [20] W.-J. Zhang, *J. Power Sources* **2011**, 196, 13.
- [21] C.-M. Park, J.-H. Kim, H. Kim, H.-J. Sohn, *Chem. Soc. Rev.* **2010**, 39, 3115.
- [22] J. R. Szczech, S. Jin, *Energy Environ. Sci.* **2011**, 4, 56.
- [23] C. K. Chan, H. Peng, G. Liu, K. McIlwrath, X. F. Zhang, R. A. Huggins, Y. Cui, *Nat. Nanotechnol.* **2008**, 3, 31.
- [24] J. Liu, K. Song, C. Zhu, C.-C. Chen, P. A. van Aken, J. Maier, Y. Yu, *ACS Nano* **2014**, 8, 7051.
- [25] W. Li, Z. Yang, J. Cheng, X. Zhong, L. Gu, Y. Yu, *Nanoscale* **2014**, 6, 4532.
- [26] M. H. Park, K. Kim, J. Kim, J. Cho, *Adv. Mater.* **2010**, 22, 415.
- [27] J. Liu, P. Kopold, P. A. van Aken, J. Maier, Y. Yu, *Angew. Chem., Int. Ed.* **2015**, 127, 9768.
- [28] A. R. Kamali, D. J. Fray, *Rev. Adv. Mater. Sci.* **2011**, 27, 14.
- [29] Y. Yu, L. Gu, X. Lang, C. Zhu, T. Fujita, M. Chen, J. Maier, *Adv. Mater.* **2011**, 23, 2443.
- [30] W. M. Zhang, J. S. Hu, Y. G. Guo, S. F. Zheng, L. S. Zhong, W. G. Song, L. J. Wan, *Adv. Mater.* **2008**, 20, 1160.
- [31] M. T. McDowell, S. W. Lee, W. D. Nix, Y. Cui, *Adv. Mater.* **2013**, 25, 4966.
- [32] X. H. Liu, Y. Liu, A. Kushima, S. Zhang, T. Zhu, J. Li, J. Y. Huang, *Adv. Energy Mater.* **2012**, 2, 722.
- [33] J. R. Dahn, T. Zheng, Y. Liu, J. Xue, *Science* **1995**, 270, 590.
- [34] B. Key, M. Morcrette, J.-M. Tarascon, C. P. Grey, *J. Am. Chem. Soc.* **2010**, 133, 503.
- [35] B. Key, R. Bhattacharyya, M. Morcrette, V. Seznec, J.-M. Tarascon, C. P. Grey, *J. Am. Chem. Soc.* **2009**, 131, 9239.
- [36] W. Liang, H. Yang, F. Fan, Y. Liu, X. H. Liu, J. Y. Huang, T. Zhu, S. Zhang, *ACS Nano* **2013**, 7, 3427.
- [37] I. A. Courtney, J. Dahn, *J. Electrochem. Soc.* **1997**, 144, 2045.
- [38] W.-J. Zhang, *J. Power Sources* **2011**, 196, 877.
- [39] N. Mahmood, Y. Hou, *Adv. Sci.* **2014**, 1, 1400012.
- [40] H. Zhao, W. Yuan, G. Liu, *Nano Today* **2015**, 10, 193.

- [41] V. Agubra, J. Fergus, *Materials* **2013**, 6, 1310.
- [42] J. Wen, Y. Yu, C. Chen, *Mater. Express* **2012**, 2, 197.
- [43] H. Maruyama, H. Nakano, M. Ogawa, M. Nakamoto, T. Ohta, A. Sekiguchi, *Sci. Rep.* **2015**, 5, 13219.
- [44] K. Zaghib, M. Simoneau, M. Armand, M. Gauthier, *J. Power Sources* **1999**, 81, 300.
- [45] C. Liu, Z. G. Neale, G. Cao, *Mater. Today* **2016**, 19, 109.
- [46] M. Green, E. Fielder, B. Scrosati, M. Wachtler, J. S. Moreno, *Electrochem. Solid-State Lett.* **2003**, 6, A75.
- [47] B. Scrosati, J. Hassoun, Y.-K. Sun, *Energy Environ. Sci.* **2011**, 4, 3287.
- [48] C. R. Becker, K. E. Strawhecker, Q. P. McAllister, C. A. Lundgren, *ACS Nano* **2013**, 7, 9173.
- [49] F. Luo, G. Chu, X. Xia, B. Liu, J. Zheng, J. Li, H. Li, C. Gu, L. Chen, *Nanoscale* **2015**, 7, 7651.
- [50] M. Nie, D. P. Abraham, Y. Chen, A. Bose, B. L. Lucht, *J. Phys. Chem. C* **2013**, 117, 13403.
- [51] S.-W. Song, S.-W. Baek, *Electrochem. Solid-State Lett.* **2009**, 12, A23.
- [52] C. K. Chan, R. Ruffo, S. S. Hong, Y. Cui, *J. Power Sources* **2009**, 189, 1132.
- [53] P. Verma, P. Maire, P. Novák, *Electrochim. Acta* **2010**, 55, 6332.
- [54] I. A. Shkrob, J. F. Wishart, D. P. Abraham, *J. Phys. Chem. C* **2015**, 119, 14954.
- [55] Z. Chen, W. Ren, L. Gao, B. Liu, S. Pei, H.-M. Cheng, *Nat. Mater.* **2011**, 10, 424.
- [56] H. He, G. Jin, H. Wang, X. Huang, Z. Chen, D. Sun, Y. Tang, *J. Mater. Chem. A* **2014**, 2, 3563.
- [57] S. Goriparti, E. Miele, F. De Angelis, E. Di Fabrizio, R. P. Zaccaria, C. Capiglia, *J. Power Sources* **2014**, 257, 421.
- [58] X. H. Liu, L. Zhong, S. Huang, S. X. Mao, T. Zhu, J. Y. Huang, *ACS Nano* **2012**, 6, 1522.
- [59] N. Lin, Y. Han, L. Wang, J. Zhou, J. Zhou, Y. Zhu, Y. Qian, *Angew. Chem., Int. Ed.* **2015**, 54, 3822.
- [60] Y. Xu, Q. Liu, Y. Zhu, Y. Liu, A. Langrock, M. R. Zachariah, C. Wang, *Nano Lett.* **2013**, 13, 470.
- [61] G. Cui, L. Gu, L. Zhi, N. Kaskhedikar, P. A. van Aken, K. Müllen, J. Maier, *Adv. Mater.* **2008**, 20, 3079.
- [62] G. Cui, Y. S. Hu, L. Zhi, D. Wu, I. Lieberwirth, J. Maier, K. Müllen, *Small* **2007**, 3, 2066.
- [63] D. Chen, X. Mei, G. Ji, M. Lu, J. Xie, J. Lu, J. Y. Lee, *Angew. Chem., Int. Ed.* **2012**, 51, 2409.
- [64] J. Liu, Y. Wen, P. A. van Aken, J. Maier, Y. Yu, *Nano Lett.* **2014**, 14, 6387.
- [65] S. Murugesan, J. T. Harris, B. A. Korgel, K. J. Stevenson, *Chem. Mater.* **2012**, 24, 1306.
- [66] Y. Zhang, Q. Fu, Q. Xu, X. Yan, R. Zhang, Z. Guo, F. Du, Y. Wei, D. Zhang, G. Chen, *Nanoscale* **2015**, 7, 12215.
- [67] Y. S. Hu, R. Demir-Cakan, M. M. Titirici, J. O. Müller, R. Schlögl, M. Antonietti, J. Maier, *Angew. Chem., Int. Ed.* **2008**, 47, 1645.
- [68] Z. Lu, N. Liu, H.-W. Lee, J. Zhao, W. Li, Y. Li, Y. Cui, *ACS Nano* **2015**, 9, 2540.
- [69] T. Kennedy, M. Brandon, K. M. Ryan, *Adv. Mater.* **2016**, 28, 5696.
- [70] G. Jeong, J.-G. Kim, M.-S. Park, M. Seo, S. M. Hwang, Y.-U. Kim, Y.-J. Kim, J. H. Kim, S. X. Dou, *ACS Nano* **2014**, 8, 2977.
- [71] J. Wang, Y. Yu, L. Gu, C. Wang, K. Tang, J. Maier, *Nanoscale* **2013**, 5, 2647.
- [72] T. H. Hwang, Y. M. Lee, B.-S. Kong, J.-S. Seo, J. W. Choi, *Nano Lett.* **2012**, 12, 802.
- [73] Y. Yu, L. Gu, C. Zhu, P. A. Van Aken, J. Maier, *J. Am. Chem. Soc.* **2009**, 131, 15984.
- [74] Y. Yu, L. Gu, C. Wang, A. Dhanabalan, P. A. van Aken, J. Maier, *Angew. Chem., Int. Ed.* **2009**, 48, 6485.
- [75] H. Wu, G. Zheng, N. Liu, T. J. Carney, Y. Yang, Y. Cui, *Nano Lett.* **2012**, 12, 904.
- [76] M.-H. Park, M. G. Kim, J. Joo, K. Kim, J. Kim, S. Ahn, Y. Cui, J. Cho, *Nano Lett.* **2009**, 9, 3844.
- [77] T. Song, J. Xia, J.-H. Lee, D. H. Lee, M.-S. Kwon, J.-M. Choi, J. Wu, S. K. Doo, H. Chang, W. I. Park, *Nano Lett.* **2010**, 10, 1710.
- [78] M. Ge, J. Rong, X. Fang, C. Zhou, *Nano Lett.* **2012**, 12, 2318.
- [79] C. K. Chan, R. N. Patel, M. J. O'connell, B. A. Korgel, Y. Cui, *ACS Nano* **2010**, 4, 1443.
- [80] A. M. Chockla, K. C. Klavetter, C. B. Mullins, B. A. Korgel, *ACS Appl. Mater. Interfaces* **2012**, 4, 4658.
- [81] C. K. Chan, X. F. Zhang, Y. Cui, *Nano Lett.* **2008**, 8, 307.
- [82] L.-F. Cui, Y. Yang, C.-M. Hsu, Y. Cui, *Nano Lett.* **2009**, 9, 3370.
- [83] H. Kim, Y. Son, C. Park, J. Cho, H. C. Choi, *Angew. Chem., Int. Ed.* **2013**, 52, 5997.
- [84] Y. Sun, S. Jin, G. Yang, J. Wang, C. Wang, *ACS Nano* **2015**, 9, 3479.
- [85] T. D. Bogart, D. Oka, X. Lu, M. Gu, C. Wang, B. A. Korgel, *ACS Nano* **2013**, 8, 915.
- [86] A. M. Chockla, J. T. Harris, V. A. Akhavan, T. D. Bogart, V. C. Holmberg, C. Steinhagen, C. B. Mullins, K. J. Stevenson, B. A. Korgel, *J. Am. Chem. Soc.* **2011**, 133, 20914.
- [87] J. Wang, N. Du, H. Zhang, J. Yu, D. Yang, *J. Mater. Chem.* **2012**, 22, 1511.
- [88] M. H. Park, Y. Cho, K. Kim, J. Kim, M. Liu, J. Cho, *Angew. Chem., Int. Ed.* **2011**, 123, 9821.
- [89] X. Wang, R. A. Susantyoko, Y. Fan, L. Sun, Q. Xiao, Q. Zhang, *Small* **2014**, 10, 2826.
- [90] L.-F. Cui, R. Ruffo, C. K. Chan, H. Peng, Y. Cui, *Nano Lett.* **2008**, 9, 491.
- [91] Y. Yao, N. Liu, M. T. McDowell, M. Pasta, Y. Cui, *Energy Environ. Sci.* **2012**, 5, 7927.
- [92] H. Wu, G. Chan, J. W. Choi, Y. Yao, M. T. McDowell, S. W. Lee, A. Jackson, Y. Yang, L. Hu, Y. Cui, *Nat. Nanotechnol.* **2012**, 7, 310.
- [93] M.-H. Seo, M. Park, K. T. Lee, K. Kim, J. Kim, J. Cho, *Energy Environ. Sci.* **2011**, 4, 425.
- [94] B. Zhu, N. Liu, M. McDowell, Y. Jin, Y. Cui, J. Zhu, *Nano Energy* **2015**, 13, 620.
- [95] E. M. Lotfabad, P. Kalisvaart, A. Kohandehghan, K. Cui, M. Kupsta, B. Farbod, D. Mitlin, *J. Mater. Chem. A* **2014**, 2, 2504.
- [96] S. C. Jung, Y.-K. Han, *J. Phys. Chem. Lett.* **2013**, 4, 2681.
- [97] S. Ohara, J. Suzuki, K. Sekine, T. Takamura, *J. Power Sources* **2004**, 136, 303.
- [98] A. A. Arie, J. O. Song, J. K. Lee, *Mater. Chem. Phys.* **2009**, 113, 249.
- [99] C. Yu, X. Li, T. Ma, J. Rong, R. Zhang, J. Shaffer, Y. An, Q. Liu, B. Wei, H. Jiang, *Adv. Energy Mater.* **2012**, 2, 68.
- [100] D. Li, K. H. Seng, D. Shi, Z. Chen, H. K. Liu, Z. Guo, *J. Mater. Chem. A* **2013**, 1, 14115.
- [101] X. Zhou, L. J. Wan, Y. G. Guo, *Adv. Mater.* **2013**, 25, 2152.
- [102] F.-W. Yuan, H.-Y. Tuan, *Chem. Mater.* **2014**, 26, 2172.
- [103] M. Liang, L. Zhi, *J. Mater. Chem.* **2009**, 19, 5871.
- [104] Z.-S. Wu, W. Ren, L. Gao, J. Zhao, Z. Chen, B. Liu, D. Tang, B. Yu, C. Jiang, H.-M. Cheng, *ACS Nano* **2009**, 3, 411.
- [105] M. D. Stoller, S. Park, Y. Zhu, J. An, R. S. Ruoff, *Nano Lett.* **2008**, 8, 3498.
- [106] H. Wang, T. Maiyalagan, X. Wang, *ACS Catal.* **2012**, 2, 781.
- [107] B. M. Bang, J. I. Lee, H. Kim, J. Cho, S. Park, *Adv. Energy Mater.* **2012**, 2, 878.
- [108] C. Xiao, N. Du, X. Shi, H. Zhang, D. Yang, *J. Mater. Chem. A* **2014**, 2, 20494.
- [109] S. Liu, J. Feng, X. Bian, Y. Qian, J. Liu, H. Xu, *Nano Energy* **2015**, 13, 651.
- [110] Z. Zhang, Y. Wang, W. Ren, Q. Tan, Y. Chen, H. Li, Z. Zhong, F. Su, *Angew. Chem., Int. Ed.* **2014**, 126, 5265.
- [111] Y. Yu, L. Gu, C. Zhu, S. Tsukimoto, P. A. van Aken, J. Maier, *Adv. Mater.* **2010**, 22, 2247.

- [112] X. Liu, J. Zhao, J. Hao, B.-L. Su, Y. Li, *J. Mater. Chem. A* **2013**, *1*, 15076.
- [113] Y. Yao, M. T. McDowell, I. Ryu, H. Wu, N. Liu, L. Hu, W. D. Nix, Y. Cui, *Nano Lett.* **2011**, *11*, 2949.
- [114] A. Esmanski, G. A. Ozin, *Adv. Funct. Mater.* **2009**, *19*, 1999.
- [115] Y. Yu, C. Yan, L. Gu, X. Lang, K. Tang, L. Zhang, Y. Hou, Z. Wang, M. W. Chen, O. G. Schmidt, *Adv. Energy Mater.* **2013**, *3*, 281.
- [116] N. Liu, Z. Lu, J. Zhao, M. T. McDowell, H.-W. Lee, W. Zhao, Y. Cui, *Nat. Nanotechnol.* **2014**, *9*, 187.
- [117] A. Magasinski, P. Dixon, B. Hertzberg, A. Kvit, J. Ayala, G. Yushin, *Nat. Mater.* **2010**, *9*, 353.
- [118] J. Wang, J.-Z. Wang, Z.-Q. Sun, X.-W. Gao, C. Zhong, S.-L. Chou, H.-K. Liu, *J. Mater. Chem. A* **2014**, *2*, 4613.
- [119] C. Zhang, S. Pang, Q. Kong, Z. Liu, H. Hu, W. Jiang, P. Han, D. Wang, G. Cui, *RSC Adv.* **2013**, *3*, 1336.
- [120] J. Qin, C. He, N. Zhao, Z. Wang, C. Shi, E.-Z. Liu, J. Li, *ACS Nano* **2014**, *8*, 1728.
- [121] G. Wang, B. Wang, X. Wang, J. Park, S. Dou, H. Ahn, K. Kim, *J. Mater. Chem.* **2009**, *19*, 8378.
- [122] C. Wu, J. Maier, Y. Yu, *Adv. Funct. Mater.* **2015**, *25*, 3488.
- [123] X. Liu, J. Cheng, W. Li, X. Zhong, Z. Yang, L. Gu, Y. Yu, *Nanoscale* **2014**, *6*, 7817.
- [124] X. Li, X. Meng, J. Liu, D. Geng, Y. Zhang, M. N. Banis, Y. Li, J. Yang, R. Li, X. Sun, *Adv. Funct. Mater.* **2012**, *22*, 1647.
- [125] X. Zhong, Z. Yang, X. Liu, J. Wang, L. Gu, Y. Yu, *ACS Appl. Mater. Interfaces* **2015**, *7*, 18320.
- [126] H. Wu, G. Yu, L. Pan, N. Liu, M. T. McDowell, Z. Bao, Y. Cui, *Nat. Commun.* **2013**, *4*, 1943, DOI:10.1038/ncomms2941.
- [127] B. Luo, L. Zhi, *Energy Environ. Sci.* **2015**, *8*, 456.
-